International Communications in Heat and Mass Transfer 175 (2026) 111104

Contents lists available at ScienceDirect

International Communications in Heat and Mass Transfer

journal homepage: www.elsevier.com/locate/ichmt

# Base-integrated thermal storage system: Enhancing phase change material melting performance through geometric innovation and artificial neural network-genetic algorithm optimization

Jun-Bo Mao [a], Ali Basem [b], Hyder H. Abed Balla [c,*], Yong-hui Li [d,*], Omar J. Alkhatib [e,*], M.A. Ahmed [f,*], Sherzod Abdullaev [g,h], Hind Albalawi [i], Zuhair Jastaneyah [j], Ibrahim Mahariq [k,l,m,n,**]

[a] School of Public Administration, Xiangtan University, Xiangtan 411105, China
[b] Advanced Technical College, University of Warith Al-Anbiyaa, Karbala, Iraq
[c] Aeronautical Technical Department, Najaf Technical Institute,Al Furat Al Awsat Technical University, Najaf, Kufa, Iraq
[d] School of Digital Economy and Management, Sichuan University of Technology and Business, Meishan, Sichuan 620000, China
[e] Architectural Engineering Department, United Arab Emirates University, Al Ain, United Arab Emirates
[f] Department of Mathematics, College of Science, Majmaah University, Al-Majmaah 11952, Saudi Arabia
[g] Senior Researcher of Scientific Department, National Pedagogical University of Uzbekistan, Tashkent, Uzbekistan
[h] Department of chemical engineering, Andijan State Technical Institute, Andijan, Uzbekistan
[i] Department of Physics, College of Sciences, Princess Nourah bint Abdulrahman University, P.O. Box 84428, Riyadh 11671, Saudi Arabia
[j] Department of Mechanical Engineering, College of Engineering, University of Business and Technology, Jeddah 21361, Saudi Arabia
[k] Department of Electrical and Electronic Engineering, Faculty of Engineering and Architecture, Istanbul Gelisim University, Avcılar- Istanbul, 34310, Istanbul, Türkiye
[l] Najjad Zeenni Faculty of Engineering, Al-Quds University, Jerusalem, Palestine
[m] Department of Medical Research, China Medical University Hospital, China Medical University, Taichung, Taiwan
[n] University College, Korea University, Seoul 02481, South Korea

ARTICLE INFO

*Keywords:*
Green energy
Thermal storage devices
Phase change materials
Melting performance
Artificial neural networks
Base and tubes

ABSTRACT

Efficient and economically viable energy storage systems are crucial for enhancing the reliability of solar-based heating applications, particularly during periods of limited sunlight availability. In this study, a novel base-integrated energy storage unit was introduced, in which heat transfer fluid tubes were embedded directly within the PCM box and supported by adjustable straight and tilted bases. This configuration enhances conductive pathways through continuous solid–solid contact among the tubes, bases, and device body, resulting in improved heat transfer performance while offering high structural flexibility and lower maintenance costs compared to conventional shell-and-tube systems. To systematically assess the influence of structural variables (the length of straight bases, the length of tilted bases, and the angle of tilted bases), a full factorial numerical analysis was carried out, generating distinct geometric designs. By the end of the 5-h charging period, the highest liquid fraction among the 27 parametric configurations was achieved by Design 5, reaching a value of 0.906, whereas the base-free design attained a liquid fraction of only 0.368. This indicates that Design 5 enhances the melting performance by approximately 146% compared to the base-free configuration. A similar trend is observed in terms of total stored energy. After 5 h, Design 5 stores 23,944 kJ of thermal energy, while the base-free system stores only 10,852 kJ. This corresponds to an improvement of approximately 120.6% in total absorbed energy for Design 5 relative to the base-free design. To generalize these findings, an artificial neural network prediction model was developed using MATLAB's feedforward network with the Levenberg–Marquardt training algorithm. The trained model was subsequently coupled with a genetic algorithm to carry out both single- and multi-objective optimization, with the goal of maximizing the PCM liquid fraction. The genetic algorithm yielded two optimal geometric configurations: **Half-Melting Optimal** for maximizing liquid fraction at 2.5 h and **Full-Melting Optimal** for maximizing liquid fraction at 2.5 h. The TOPSIS-selected design, named

* Corresponding authors.
** Corresponding author at: University College, Korea University, Seoul 02481, South Korea.
*E-mail addresses:* hyderballa@atu.edu.iq (H.H. Abed Balla), gytfb588@126.com (Y.-h. Li), omar.alkhatib@uaeu.ac.ae (O.J. Alkhatib), moh.hassan@mu.edu.sa (M.A. Ahmed), Ibmahariq@gmail.com (I. Mahariq).

https://doi.org/10.1016/j.icheatmasstransfer.2026.111104

Available online 26 March 2026

Balanced-Melting Optimal, falls between the values of Half-Melting Optimal and Full-Melting Optimal. Besides, three additional engineered Finned-designs were introduced to be compared with the optimal designs. After 5 h of charging, the liquid fraction reached 0.847, 0.913, and 0.881 for Half-Melting Optimal, Full-Melting Optimal, and Balanced-Melting Optimal, respectively. These values correspond to improvements of 130%, 148%, and 139%, respectively compared to the base-free design. Besides, Half-Melting Optimal, Full-Melting Optimal, and Balanced-Melting Optimal stored 23,236 kJ, 24359 kJ, and 23,810 kJ, respectively, compared to 10,852 kJ for the base-free system, yielding improvements of approximately 114%, 124%, and 120%. Among the optimized configurations, Full-Melting Optimal was proposed as the best overall optimal design, since it achieved the highest performance in terms of both liquid fraction and total stored energy. When compared directly with Design 5, the Full-Melting Optimal configuration still provided measurable improvements, with approximately 0.77% betterment in liquid fraction and about 1.73% in stored energy.

**Nomenclature**

| | |
|---|---|
| $C_p$ | specific heat (kJ/kg·K) |
| $E_m$ | melting enhancement ratio (%) |
| $F$ | latent enthalpy of melting (kJ/kg) |
| $g$ | gravitational acceleration (m/s$^2$) |
| $\Delta H$ | latent enthalpy (kJ/kg) |
| $H$ | specific enthalpy (kJ/kg) |
| $h$ | sensible enthalpy (kJ/kg) |
| $I$ | characteristic height (m) |
| $k$ | thermal conductivity (W/m·k) |
| $L_{SB}$ | length of straight bases (mm) |
| $L_{TB}$ | length of tilted bases (mm) |
| $M_{rf}$ | mushy region parameter |
| $P$ | pressure (Pa) |
| $t$ | time (s) |
| $V$ | velocity (m/s) |
| $\varepsilon$ | small regularization constant |
| $\alpha$ | source term |
| $\varphi$ | liquid fraction |
| $\theta$ | angle of tilted bases (degree) |
| $\rho$ | density (kg/m$^3$) |
| $\mu$ | dynamics viscosity (kg/m·s) |
| $\gamma$ | coefficient of thermal expansion (1/K) |

*Abbreviations*

| | |
|---|---|
| ANN | artificial neural networks |
| HTF | heat transfer fluid |
| GA | genetic algorithm |
| PCM | phase change material |
| TSD | thermal storage device |

## 1. Introduction

The global shift toward green energy has accelerated the integration of renewable sources such as solar, wind, and biomass into modern power systems [1]. While these technologies significantly reduce reliance on fossil fuels, their fluctuating and unpredictable nature demands effective storage solutions to balance supply and consumption [2]. Energy storage methods are generally classified into three categories: mechanical, electrochemical, and thermal [3]. Mechanical storage, including pumped hydro and compressed air, offers large-scale capacity but is limited by geographical and infrastructural constraints [4]. Electrochemical storage, primarily batteries, delivers high efficiency and rapid response but faces challenges related to cost, limited lifespan, and environmental concerns [5]. Thermal storage devices (TSDs), in contrast, provide a more economically favorable pathway, capable of storing excess energy as sensible, latent, or thermochemical heat [6]. Its direct compatibility with solar systems and wide range of applications make TSDs particularly attractive for addressing the requirements of a sustainable energy future [7].

Among the available TSDs, latent heat storage using phase change materials (PCMs) has been in the spotlight due to its ability to provide high energy density while operating within narrow temperature intervals [8]. PCMs are capable of storing and releasing large amounts of heat during phase transition reversibly and predictably [9]. This makes them highly suitable for integration with thermal management of electronic devices, building climate control, and concentrated solar power plants [10]. Despite these advantages, the practical deployment of PCMs is often hindered by their insufficient thermal conductivity, which limits the rate of heat transfer and reduces system efficiency [11]. Consequently, there are increasing efforts to develop various enhancement strategies that unlock the full potential of PCM-based mechanisms [12]. The techniques can be divided into material-level modifications and structural-level modifications [13]. The first category involves altering the PCM itself, for instance, by dispersing nanoparticles or embedding high-conductivity additives to accelerate heat diffusion [14]. While such approaches are effective in improving thermal conductivity, they commonly diminish the effective latent heat storage capacity and may raise long-term stability issues [15]. The second category focuses on modifying the storage structure, for example by incorporating metal or graphite foams, porous matrices, and encapsulation techniques to facilitate heat transport within the PCM domain [16]. Such approaches are effective in enhancing thermal performance; however, they are often associated with increased manufacturing complexity, higher cost, and added design constraints [17]. It should be noted that metal and graphite foams can be fabricated using established techniques and are not inherently impractical. Nevertheless, when compared with porous structures, extended surfaces such as fins offer notable advantages in terms of simplicity and controllability [18]. In particular, fins provide greater geometric flexibility, easier integration into conventional fabrication processes, and more precise control over key design parameters, including length, thickness, orientation, and spacing [19]. By contrast, foam-based structures typically introduce additional considerations related to pore size distribution, permeability, flow resistance, and PCM–solid contact resistance, which can complicate both numerical modeling and systematic optimization. Given these considerations, the integration of auxiliary or extended surfaces has emerged as a desirable and practical alternative for enhancing heat transfer in thermal energy storage systems [20]. Although extended surfaces reduce the available PCM volume, they can significantly enhance heat transfer rates and shorten charging/discharging times, which is often more critical for practical thermal energy storage applications than maximizing theoretical latent heat capacity alone [21]. This distinctive advantage has positioned extended surfaces at the center of recent research [22].

Wang et al. [23] introduced an innovative fin design by combining longitudinal straight fins with arc-shaped fractal fins in a storage unit.

They assessed the impact of fin curvature, curvature size, and spacing on melting characteristics. The findings revealed that negatively curved fins provided superior charging efficiency, with the 90° fractal fin achieving the best performance by shortening the complete melting time by 34.27% compared to straight fins. Moreover, gradually decreasing the spacing of fractal fins from the lateral to the medial region enhanced phase transition uniformity, leading to a 2.5% reduction in total melting time and a 2.57% improvement in energy storage rate. He et al. [24] developed topological fin structures to maximize the thermal energy absorption in a storage system. Simulations were carried out under two operating conditions: 90–60 °C and 85–65 °C. In the first case, the topological fins improved heat transfer efficiency by 57.8% compared with a finless setup and by 25.3% compared with rectangular fins. In the second case, the proposed design maintained its advantage, achieving improvements of 67.5% and 22.8% over fin-free and rectangular fin systems, respectively. Tang et al. [25] investigated the impact of geometric parameters of discontinuous fins on the melting dynamics of a TSD. It was highlighted that fin length and bifurcation angle are the dominant factors, especially during early melting stages. For fin lengths greater than 15 mm, the impact of bifurcation angle on melting time diminished, while longer fins generally slowed the melting rate. Compared with traditional straight fins, the optimal configuration decreased melting time by approximately 31% at a liquid fraction of 0.9 and by 21% at complete melting. Abdulrazzaq et al. [26] modified a heat storage system by applying multi-branch fins to enhance melting and solidification performance. The study tested four structures, namely plain fins, two-branch fins, four-branch fins, and five-branch fins. The results showed that adding branches improved melting rates by increasing the heat transfer area, with the two-, three-, and four-branch fins reducing melting time from 90 to 60 min. However, the five-branch structure offered minimal additional benefit due to fin crowding. Similar improvements were also observed during solidification, with multi-branch fins shortening the process by 18 to 29%. Marzouk et al. [27] examined a pin finned-TSD to inspect the thermal capabilities of a PCM. The authors examined fin length ratios of 1, 2, 3, and 4 and compared them with a reference model that did not have fins. The data showed that a fin length ratio of 4 significantly enhanced system performance, increasing overall liquid fraction and average temperature by 67% and 29%, respectively. Additionally, the complete melting time was reduced by 61.5% with a fin ratio of 4 compared to the reference system.

With the growing sophistication of TSDs, conventional evaluation methods frequently encounter considerable drawbacks [28]. They are often burdened by high resource demands, limited adaptability to geometric modifications, and slow responsiveness when addressing complex operational scenarios [29]. Such challenges restrict the efficiency in exploring wide design spaces or achieving rapid optimization [30]. By contrast, artificial neural networks (ANNs) provide a flexible, data-driven alternative that can uncover intricate nonlinear patterns and deliver reliable predictions with minimal computational overhead [31]. This capability has encouraged researchers to increasingly employ ANN-based approaches in their studies [32]. Li et al. [33] examined a TSD to determine the PCM melt fractions during 3-h and 6-h energy absorption periods. Two configurations that maximized melting performance within the respective durations were obtained via ANN. The first design, optimized for the 3 h, achieved a remarkable 103.11% increase in liquid fraction, while the second configuration, optimized for the 6 h, provided a 98% improvement compared to the baseline. Yan et al. [34] applied an ANN framework to forecast the solidification behavior of RT50 in a finned-triplex-tube storage unit. The prediction model considered geometric parameters such as outer fin arc angle, inner fin arc angle, and fin spacing as inputs to identify the optimal model that accelerated the discharging process. The outcomes demonstrated that the optimized case reduced the time to reach a liquid fraction of 0.1 by more than 80% compared with a no-fin design. Almadhor et al. [35] used two ANN models to anticipate the time required for 50% and 100% PCM melting in a TSD supported by stands. It was found that in the reference setup without stands, about 8515 s were needed to reach half melting, and over 18,000 s were required for complete melting. In contrast, the prediction models improved system performance: one reduced the half-melting time by 62.5%, while the other achieved complete melting in nearly half the time.

To address the limitations of conventional latent heat storage geometries, this study introduces a base-integrated thermal energy storage architecture that is fundamentally different from traditional shell-and-tube or finned-tube configurations. In conventional shell-and-tube systems, the HTF tubes are mounted independently inside the shell and fixed via tube sheets, resulting in discontinuous solid contact between the tubes and the surrounding structure. This separation restricts conductive heat transfer and introduces additional thermal resistance between the heat source and the PCM. In contrast, the proposed system integrates the tubes, supporting bases, and storage body into a single continuous solid structure, establishing uninterrupted solid–solid contact throughout the device. This integration creates an extended conductive heat transfer pathway that penetrates deeply into the PCM volume, rather than relying primarily on convective enhancement or localized fin effects. As a result, thermal resistance is reduced and heat is distributed more uniformly within the PCM, leading to accelerated and more homogeneous melting. A further distinguishing feature of the proposed design is its specific construction, in which the storage system is composed of compact, self-contained unit. This structure enables straightforward transportation, on-site assembly, and flexible scaling of storage capacity without altering or replacing the embedded tubes, an advantage not achievable in conventional shell-and-tube or finned-tube storage systems. Moreover, the system offers geometric reconfigurability through bases of adjustable length and inclination, allowing precise control over tube positioning within the PCM enclosure. By combining straight and tilted bases, the conductive heat transfer network can be actively tailored to accelerate the melting process. This study couples such a base-integrated storage geometry with an ANN model and genetic algorithm–based optimization to identify optimal tube arrangements that maximize PCM liquid fraction within specified charging durations.

## 2. Methodology

### 2.1. Design features of the base-integrated storage system

Fig. 1 schematically presents the experimental loop designed to evaluate the charging performance of the proposed TSD. The loop consists of four main subsystems: a solar heat collection unit, an HTF circulation loop, the PCM-based energy storage module, and a domestic hot water supply loop. The solar collector serves as the primary heat source and is responsible for heating the HTF during the charging process. The HTF, flowing through insulated pipes, absorbs thermal energy from the collector and is directed toward the energy storage unit. The

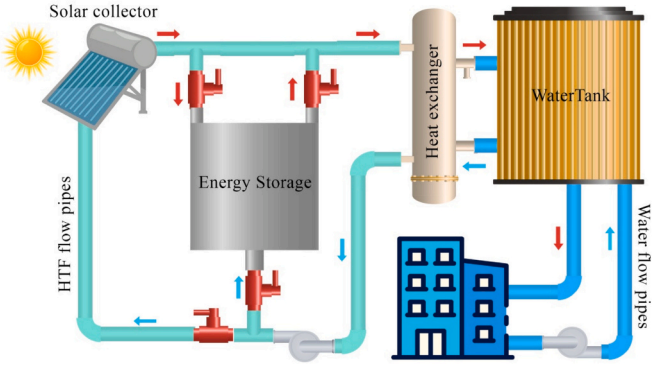


**Fig. 1.** The closed-loop cycle of a solar-assisted energy storage system.

HTF circulation is controlled using valves and a pump to regulate the flow direction and flow rate, ensuring stable and repeatable operating conditions. The energy storage unit, located downstream of the solar collector, contains the PCM and the internally embedded tube-base heat transfer structure investigated in this study. Hot HTF enters the storage unit through the upper inlet and transfers heat to the PCM via conduction through the tube walls and bases, as well as natural convection within the molten PCM region. The cooled HTF exits the storage unit and is recirculated back to the solar collector, completing the closed HTF loop. To simulate a practical domestic application, the stored thermal energy is delivered to a water heating subsystem through a heat exchanger. In this section, the hot HTF exiting the energy storage unit transfers its thermal energy to water flowing through a separate loop connected to a water tank. The heat exchanger ensures indirect heat transfer between the HTF and water, preventing fluid mixing while maintaining efficient energy exchange. The water circulation loop supplies heated water to the consumer side and returns cooler water back to the tank for reheating. Directional arrows in Fig. 1 indicate the flow paths of both HTF and water during the charging and heat delivery processes. Control valves placed at strategic locations allow switching between operating modes and facilitate system isolation during experimental measurements.

The geometry of the energy storage system used in the cycle is illustrated in Fig. 2a. The configuration consists of a cylindrical PCM enclosure containing HTF tubes that are supported and stabilized by straight and tilted bases. The design also includes two detachable end covers, allowing multiple intermediate storage sections to be mechanically connected between them when larger storage capacity is required. In this concept, additional sections can be attached in series using bolts, while the inlet and outlet remain sealed by the end covers. In this configuration, the HTF flow rate is assumed to remain constant, meaning that the same volumetric flow enters and exits the system regardless of the number of connected sections. Increasing the system length primarily leads to a gradual reduction in HTF temperature along the flow direction, which decreases the local temperature difference between the HTF and PCM in downstream sections. For the present numerical model, axial temperature variations were found to be significantly smaller than radial variations and were therefore neglected in the simplified 2D simulations. However, as the total system length increases, axial temperature gradients become more noticeable, meaning that the overall heat storage performance would not necessarily scale linearly with the number of connected sections. In addition, extending the system length would increase the pressure drop along the HTF tubes due to additional friction losses. Although this effect is not explicitly modeled in the present work, it represents an important consideration for longer systems. Therefore, the purpose of introducing this sectional structure is not to imply unrestricted performance scalability, but rather to highlight the practical flexibility of the design, which allows the storage capacity to be adjusted by adding or removing sections without requiring a complete redesign of the tube network or PCM enclosure. The cross-sectional schematic in Fig. 2b details the computational region adopted for numerical simulations, highlighting eight HTF tubes and their connection to the surrounding bases. The input geometric parameters used for training the ANN are explicitly shown in Fig. 2b. In the illustrated configuration of Fig. 2b, the tilted-base angle ($\theta$) is shown as $\theta = 90°$. This graphical representation now makes the definition of the tilted-base angle unambiguous. Other values of $\theta$ (e.g., 60° and 120°) correspond to rotations of the same tilted-base elements with respect to the radial direction and are employed parametrically in the ANN input space and optimization process. Since lauric acid is selected as the PCM, its relatively poor thermal conductivity presents a limitation for rapid heat distribution during the charging cycle. To address this issue, the configuration and arrangement of the bases are designed not only to enlarge the heat transfer surface area but also to promote more uniform heat distribution toward the central region of the PCM, where heat transfer is typically slower. On the other hand, the solid connections formed by the bases contribute to the structural rigidity of the storage unit, maintaining the geometric stability of the tubes during repeated thermal cycling. For the simulations, the enclosure was prescribed a longitudinal dimension of 700 mm, and aluminum is considered for

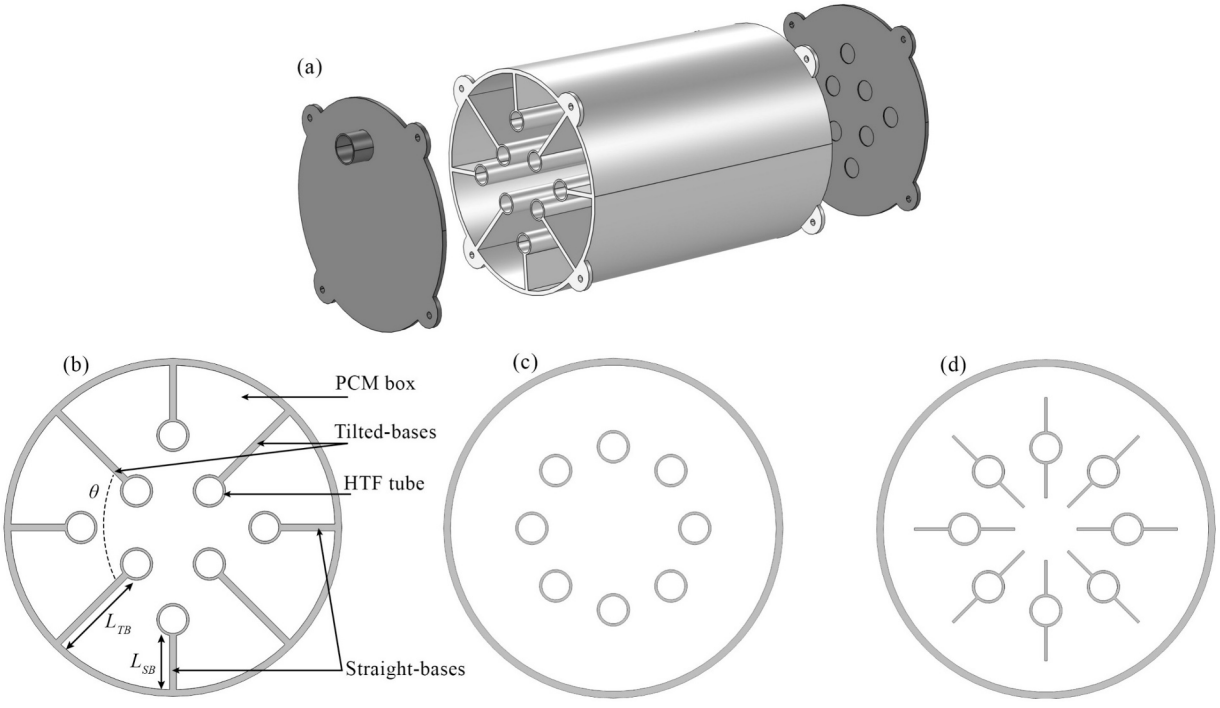


**Fig. 2.** (a) The geometry of the base-integrated storage system; (b) Cross-sectional view of the PCM box including HTF tubes and bases, showing the geometric input parameters used for ANN modeling: straight-bases length ($L_{SB}$), tilted-bases length ($L_{TB}$), and tilted-bases angle ($\theta$) (illustrated here for $\theta = 90°$); (c) Base-free reference configuration of the PCM storage unit. HTF tubes are positioned at the mid-radius of the box; (d) Finned reference configuration with the same tube positions as the base-free design. Two straight fins are attached to each tube (illustrated here for fin length of 50 mm).

fabricating the bases and all solid elements. The geometrical parameters of the base-integrated storage system are summarized in Table 1. Fig. 2c indicates the base-free design in which, the HTF tubes are located at the mid-radius of the PCM box. The box radius is 240 mm, and therefore the tube centers are positioned at a radius of 120 mm from the center of the box. This placement is intentionally chosen to be neither very close to the center nor too close to the outer wall and represents a neutral and commonly used tube arrangement in cylindrical shell-and-tube PCM storage units. Besides, three additional engineered reference designs are introduced herein. They are considered as follows:

➢ Finned-design 15: fin length = 15 mm
➢ Finned-design 50: fin length = 50 mm
➢ Finned-design 80: fin length = 80 mm

Specifically, Fig. 2d presents the finned-design 50, in which the tube positions are kept identical to the base-free configuration, and simple straight fins are attached symmetrically to each tube (one fin toward the box center and one toward the outer wall). These fin lengths are not selected arbitrarily. Rather, the fin penetration lengths are chosen in proportion to the base penetration lengths used in the present study. In the proposed system, the base lengths vary as 30 mm, 100 mm, and 160 mm, and the fin lengths are scaled accordingly to maintain a comparable order of heat transfer surface extension. The base-free design and the three finned-designs therefore constitute a set of reasonable engineering baselines, which are compared against the optimal designs introduced in this research.

### 2.2. Assumptions

Since the system under investigation focuses on energy absorption within the PCM region, a set of assumptions is necessary to ensure the reliability of the mathematical model. The list of items is provided as follows:

1. Model characteristics

- The flow is treated as incompressible.
- Heat transfer and fluid flow are represented using a time-dependent approach.
- According to several previously published numerical and experimental studies on PCM systems, axial temperature variations are typically on the order of 2.5% of the radial temperature differences [36,37] and can therefore be reasonably neglected when the focus is on phase-change behavior and radial heat transfer mechanisms. Therefore, to maintain a balance between physical fidelity and computational feasibility, the present study adopts a 2D modeling approach.

2. Material properties

- The PCM is assumed to behave as a homogeneous and isotropic medium in both solid and liquid states.
- Material properties are assumed constant within each phase (solid or liquid) throughout the simulations (Table 2). In the present simulations, the density of the PCM is treated differently in the solid and liquid regions. For the solid PCM, a constant solid density is used up to the onset of melting. After melting begins, buoyancy-driven flow in the liquid PCM is modeled using the Boussinesq approximation. In this formulation, density variations are neglected in all governing equations except for the gravitational term of the momentum equation, where they are expressed as a linear function of temperature to account for natural convection. Since the Boussinesq approximation is applied to the liquid phase, the liquid PCM density is used as the reference density in the formulation (885 kg/m$^3$).

3. Flow and heat transfer considerations

- The effect of viscous dissipation is neglected.
- Gravitational acceleration is assumed to be 9.81 m/s$^2$.
- The flow regime is considered laminar, as the Rayleigh number (*Ra*) within the PCM box remains below $10^9$.

A dedicated uncertainty and sensitivity analysis has been conducted, and the results are presented in Table 3. This table quantifies the effect of uncertainties in key thermophysical properties of the liquid PCM and selected boundary/operating parameters on the predicted melting performance at two representative times. Specifically, each parameter listed in the table was individually perturbed by ±5% around its base value, while all other parameters were kept constant. The corresponding variations in the predicted melting performance were then quantified and reported as percentage changes. This approach provides a first-order local sensitivity assessment and allows identification of the most influential parameters affecting the model outputs. As shown in Table 3, among all investigated parameters, the HTF temperature ($T_{HTF}$) exhibits the largest influence on system performance, with variations of up to ±14.1% at 2.5 h and ± 13.9% at 5 h, highlighting the dominant role of boundary thermal conditions on PCM melting behavior. In contrast, uncertainties in thermophysical properties lead to relatively minor deviations (generally below ±1–3%), indicating that the model predictions are comparatively robust with respect to moderate uncertainties in material properties. This uncertainty analysis demonstrates that while the numerical results are sensitive to HTF operating conditions, the conclusions drawn regarding the comparative performance of different designs and configurations remain stable under reasonable variations in thermophysical parameters.

### 2.3. Data reduction

The *Ra* expresses the balance between buoyancy-driven flow and diffusive resistance, making it a key parameter in PCM-based units. It directly influences the vigor of convective circulation in the molten region, thereby controlling heat transfer efficiency and the uniformity of melting fronts. This parameter can be written as follows [41]:

**Table 1**
The geometrical parameters of the base-integrated storage system.

| Geometric parameter | Value | Unit |
|---|---|---|
| PCM enclosure length | 700 | mm |
| PCM enclosure inner diameter | 480 | mm |
| PCM enclosure thickness | 10 | mm |
| HTF tube inner diameter | 40.894 | mm |
| HTF tube thickness | 3.683 | mm |
| Tube base thickness | 10 | mm |
| Straight-bases length ($L_{SB}$) | 30–160 | mm |
| Tilted-bases length | 30–100 | mm |
| Tilted-bases angle ($\theta$) | 60–120 | degree |
| HTF tubes number | 8 | – |
| Fins length | 15, 50, 80 | mm |
| Fins thickness | 3.683 | mm |

**Table 2**
The thermo-physical characteristics of the applied materials.

| Characteristics | Lauric acid [38,39] | Aluminum [40] |
|---|---|---|
| $\rho$, solid / liquid (kg/m$^3$) | 940 / 885 | 2700 |
| $C_p$, solid / liquid (kJ/kg·K) | 2.180 / 2.390 | 0.917 |
| $k$, solid / liquid (W/m·K) | 0.160 / 0.140 | 238 |
| $\mu$ (kg/m·s) | 0.006 | – |
| $\gamma$ (1/K) | $8 \times 10^{-4}$ | – |
| $F$ (kJ/kg) | 187.210 | – |
| $T_m$ (K) | 316.65–321.35 | – |

**Table 3**
Sensitivity and uncertainty analysis of thermophysical properties and boundary conditions.

| Parameter | Base case values | Range of changes | Changes in performance | |
|---|---|---|---|---|
| | | | $\varphi_{2.5h}$ | $\varphi_{5h}$ |
| $\rho$ (kg/m$^3$) | 885 | ±5% | ±2.800% | ±2.955% |
| $\mu$ (kg/m·s) | 0.006 | ±5% | ±0.747% | ±1.180% |
| $\gamma$ (1/K) | $8 \times 10^{-4}$ | ±5% | ±0.763% | ±0.901% |
| $k$ (W/m·K) | 0.14 | ±5% | ±2.669% | ±2.005% |
| $C_p$ (kJ/kg·K) | 2.390 | ±5% | ±0.705% | ±0.790% |
| $g$ (m/s$^2$) | 9.81 | ±5% | ±0.950% | ±0.993% |
| $P_{ambiant}$ (Pa) | 101,325 | ±5% | ±0.246% | ±0.601% |
| $T_{initial}$ (K) | 298.15 | ±5% | ±1.403% | ±0.900% |
| $T_{HTF}$ (K) | 333.15 | ±5% | ±14.121% | ±13.855% |

$$Ra = \frac{g\gamma C_p \rho^2 (T_{HTF} - T_{PCM}) I^3}{\mu k} \tag{1}$$

The system is governed by the conservation equations defined in Eqs. (2)–(5). In Eq. (2), the continuity equation is solved for the liquid phase [42].

$$\rho_{0,l}(\nabla . V) = 0 \tag{2}$$

Eq. (3) is the Navier–Stokes equation with two important modeling choices: (a) Boussinesq approximation: density changes are neglected except in the buoyancy term, $\rho g$, linearized via the thermal expansion coefficient $\gamma$. This dramatically reduces cost and is valid when temperature-induced density differences are moderate. (b) Momentum source $\alpha$: this term models the flow resistance introduced by the partially/fully solid PCM (mushy zone). In the enthalpy–porosity method, $\alpha$ forces velocity to near zero in solid regions [43].

$$\rho_{0,l}\left(\frac{\partial V}{\partial t} + V.\nabla V\right) = -\nabla P + \mu \nabla^2 V + g\rho_{0,l}(1 - \beta(T - T_0)) + \alpha \tag{3}$$

The energy relation in Eq. (4) is written for total enthalpy $H$, so that latent heat is incorporated naturally. The left-hand side contains transient and advective transport of enthalpy; the right-hand side represents conductive heat flux. Using enthalpy rather than a temperature-only formulation is essential for an accurate phase-change simulation because latent heat exchanges are captured in $H$ [44].

$$\rho_{0,l}\left(\frac{\partial H}{\partial t} + V.\nabla H\right) = k_l \nabla^2 T \tag{4}$$

In regions where the velocity is fully solid (zero velocity), the energy transport reduces to transient conduction, and Eq. (5) illustrates the related behavior of the system [45].

$$\rho_s \frac{\partial H}{\partial t} = k_s \nabla^2 T \tag{5}$$

Total enthalpy is the sum of sensible enthalpy $h$ and latent enthalpy $\Delta H$. This split is the core idea behind enthalpy-based phase-change modeling: $h$ tracks temperature-dependent sensible energy, while $\Delta H$ accounts for phase-change energy storage/release [46].

$$H = h + \Delta H \tag{6}$$

Sensible enthalpy is computed by integrating specific heat $C_p$ from a reference temperature. Representing $h$ in this integral form allows for a temperature-dependent $C_p$ if needed and ensures a consistent linkage between temperature and enthalpy [47].

$$h = h_{ref} + \int_{T_{ref}}^{T} C_p dT \tag{7}$$

Latent enthalpy is set proportional to the liquid fraction $\varphi$ and the latent heat L. This linear relation means that when $\varphi$ goes from 0 to 1, the material absorbs/releases the full latent heat [48].

$$\Delta H = \varphi F \tag{8}$$

The liquid fraction maps temperature onto the solid–liquid mixture fraction using linear interpolation between the solidus temperature $T_s$ and liquidus temperature $T_l$. This mushy-zone model gives a continuous transition that is numerically robust; its smoothness avoids sharp discontinuities in enthalpy, which would cause convergence problems. Choosing a finite melting range [$T_s$, $T_l$] also mimics materials that melt over a range and helps capture latent-heat absorption during the isothermal-like phase [49].

$$\varphi = \begin{cases} 0 & if \quad T_{PCM} < T_s \\ \dfrac{T_{PCM} - T_s}{T_l - T_s} & if \quad T_s \le T_{PCM} \le T_l \\ 1 & if \quad T_{PCM} > T_l \end{cases} \tag{9}$$

Here, the phase change process is modeled using the enthalpy–porosity technique. In this method, the solid PCM region is treated as a porous medium with very large momentum resistance, which suppresses velocity in solid regions and gradually allows fluid motion as the liquid fraction increases. Consequently, the solid PCM does not behave as a freely moving body, and phenomena such as detachment and sinking of solid fragments under gravity cannot be captured within this modeling framework. This limitation is inherent to the enthalpy–porosity method and has been widely reported in the literature. However, since the dominant mechanisms governing the melting process in latent heat storage systems are heat conduction and buoyancy-driven natural convection in the liquid PCM, the enthalpy–porosity approach remains a reliable and widely used method for predicting melting dynamics and liquid fraction evolution. The average PCM temperature ($T_{PCM}$) is not obtained through a separately derived analytical or empirical mathematical expression. Instead, it is directly extracted from the numerical results of the CFD simulations conducted using ANSYS Fluent. Specifically, $T_{PCM}$ is calculated in the post-processing stage as a volume-averaged temperature of the PCM domain. ANSYS Fluent internally computes this quantity based on the resolved transient temperature field by integrating the local temperature values over the entire PCM volume at each time step and dividing by the total PCM volume. Eq. (10) damps velocity in regions with low liquid fraction. In the enthalpy–porosity approach, the drag is proportional to velocity and controlled by a coefficient $A(\varphi)$. Physically, this model represents a porous-like resistance within the partially melted material, causing the flow to cease in solid zones while allowing flow in liquid regions [50].

$$\alpha = -A(\varphi)V \tag{10}$$

Eq. (11) prescribes the rate at which the drag increases as $\varphi$ decreases. $M_{rf}$ is the mushy region factor, and $\varepsilon$ is a small regularization constant to prevent division by zero when $\varphi$ is small. The functional form enforces nearly infinite resistance as $\varphi \to 0$ (solid), while $A(\varphi)$ tends to a small value as $\varphi \to 1$ (liquid) [51].

$$A(\varphi) = M_{rf}\frac{(1 - \varphi)^2}{\varphi^3 + \varepsilon} \tag{11}$$

The percentage improvement in liquid fraction of any base-integrated design relative to the base-free reference is quantified using the melting enhancement ratio $E_m$. This single-number metric makes it straightforward to compare the melting acceleration achieved by different geometries and is particularly useful when summarizing the results of many simulations in parametric or optimization studies [52].

$$E_m = \left[\frac{\varphi}{\varphi_{bf}} - 1\right] \times 100\% \tag{12}$$

To completely solve the applied equations, appropriate boundary and initial conditions are specified. The system pressure is fixed at 1 atm,

consistent with ambient conditions, and to avoid introducing compressibility effects into the incompressible flow regime. At each solid–fluid interface, the velocity is set to zero and thermal continuity is maintained, which reflect the physical behavior of viscous flow and heat transfer across contact surfaces. The HTF tube wall temperature is maintained at 333.15 K. For the initial condition, both the solid structures and the PCM domain are uniformly set to 298.15 K, corresponding to a state below the melting temperature of the PCM. This initialization guarantees that the melting process, including conduction-dominated and convection-enhanced stages, can be accurately captured throughout the simulation.

### 2.4. Solution strategy

In modeling the base-integrated storage system, the governing equations are solved using ANSYS Fluent, a computational fluid

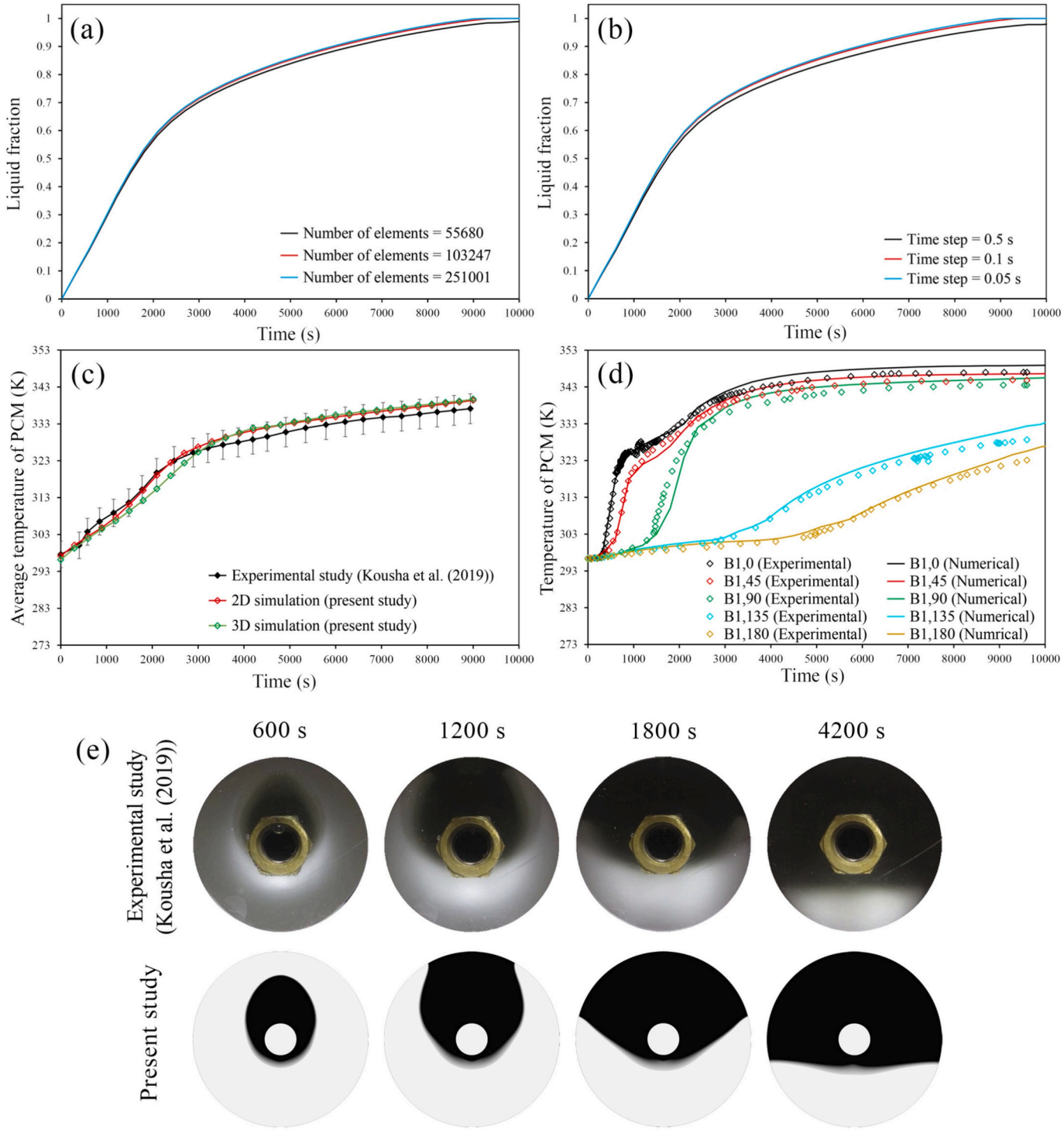


**Fig. 3.** The (a) grid independence and (b) time-step independence analyses conducted specifically for the validation case. A comparison of the (c) the evolution of average PCM temperature, alongside an additional three-dimensional simulation of the reference experimental configuration and (d) temperature data between the experimental visualization and the current simulation. (e) The evolution of the melting front.

dynamics solver that employs the finite volume method. In this approach, the computational domain is discretized into control volumes, and the conservation equations for mass, momentum, and energy are integrated over each volume. This ensures local conservation of fluxes and provides resolution of phase change and convection phenomena within the PCM. To achieve precise convergence, a combination of numerical schemes and control parameters is introduced as follows:

- ➢ The coupling between the velocity and pressure fields is achieved using the SIMPLE method.
- ➢ The momentum and energy equations are discretized using a second-order upwind approach.
- ➢ The PRESTO scheme is employed for pressure interpolation.
- ➢ Under-relaxation factors are considered below to stabilize convergence:
  - Density = 1
  - Energy = 1
  - Pressure = 0.3
  - Momentum = 0.7
  - Liquid fraction = 0.9
- ➢ Iterations are continued until the residuals of all equations drop below $10^{-6}$.

### 2.5. Model verification

Fig. 3a and b present the grid independence and time-step independence analyses conducted specifically for the validation case corresponding to the experimental configuration reported by Kousha et al. [53]. In Fig. 3a, three different mesh resolutions (55,680, 103247, and 251,001 elements) are examined by comparing the temporal evolution of the PCM liquid fraction. As shown, the liquid fraction curves obtained with 103,247 and 251,001 elements are nearly indistinguishable over the entire melting period, while a small deviation is observed for the coarsest mesh, particularly at later times. This indicates that the numerical solution becomes mesh-independent beyond approximately 100,000 elements. Therefore, the mesh with 103,247 elements was selected as an optimal compromise between numerical accuracy and computational cost for the validation simulations. Similarly, Fig. 3b illustrates the time-step independence study for the same experimental geometry, in which three time-steps were tested. The findings indicate that decreasing the time-step from 0.1 s to 0.05 s leads to negligible changes in the predicted liquid fraction, while the largest time-step of 0.5 s introduces minor discrepancies. Hence, a time-step of 0.1 s was adopted for the validation simulations, as it ensures temporal convergence of the solution while maintaining reasonable computational efficiency. These two analyses confirm that the numerical predictions reported in the validation section are independent of both mesh size and time-step for the experimental configuration.

To ensure that the adopted numerical model can accurately replicate the physical behavior of the base-integrated storage system, a verification study is essential. Accordingly, the outcomes obtained in the present investigation are validated against the experimental data reported by Kousha et al. [53]. It is well established that the evaluation of heat storage technologies is highly sensitive to the treatment of the mushy region and its factor ($M_{rf}$). Herein, an $M_{rf}$ of $10^6$ is applied, which is sufficiently large to suppress unphysical convection within the solid PCM while still enabling realistic flow development in the liquid phase. This choice provides a balanced representation of the solid–liquid interface, ensuring a smooth phase transition during the energy absorption process. In the validation study, the numerical model was adapted to exactly match the experimental conditions reported in the reference work. Specifically, the PCM used in the experimental study was RT35, which was also adopted in the present simulations for validation. The PCM enclosure diameter and HTF tube diameter were set to 70 mm and 12.5 mm, respectively, in accordance with the experimental setup. The HTF inlet temperature was 80 °C, while the initial temperature of the PCM domain was 24 °C. Regarding the thermal boundary condition, the tube wall temperature in the numerical model was prescribed based on the HTF inlet temperature, consistent with the experimental configuration in which the HTF temperature remains nearly uniform along the tube length. All geometric parameters, boundary conditions, and thermophysical properties reported in the experimental work were applied identically in the present numerical model. To account for buoyancy-driven natural convection in the liquid PCM, the thermal expansion coefficient was adopted as a value of $6 \times 10^{-4}$ 1/K, which is commonly used for RT35 in similar phase-change and natural convection studies [54].

In the validation section, the "average temperature of PCM" used for comparison was extracted from Fig. 10 of the reference experimental study for the single-tube case, which represents the average temperature measured by the thermocouples placed at five distinct locations within the PCM domain. Accordingly, the numerical average temperature reported in Fig. 3c of the present manuscript corresponds to the temperature averaged at the same five monitoring locations used in the experiment, rather than the spatially averaged PCM temperature. The data demonstrates good agreement in terms of both liquid fraction and average temperature of PCM. Furthermore, Fig. 11a of the reference experimental paper was also examined. To further examine the effect of temperature difference, an additional 3D simulation of the reference experimental configuration was performed and reported in Fig. 3c. In this model, the HTF flow inside the tube was explicitly solved by simultaneously solving the continuity, momentum, and energy equations. Unlike the simplified constant-temperature boundary condition used in the 2D PCM simulations, the HTF temperature was allowed to evolve along the flow direction, thereby capturing the axial temperature variation inside the HTF. As shown in Fig. 3c, the average PCM temperature predicted by the 3D simulation agrees closely with the 2D results, indicating that the axial temperature variation of the HTF has only a limited influence under the conditions of the reference case. At the beginning of the charging process, the 2D prediction is slightly higher than the 3D result. This occurs because, in the 3D model, the HTF experiences a small temperature decrease along the flow direction, which slightly reduces the local driving temperature difference between the tube wall and the PCM and therefore reduces the heat transfer rate reaching the PCM. In the 2D model, however, the wall temperature remains constant, so the PCM receives slightly higher thermal energy during the early stage of melting. As the charging process continues, the 2D and 3D temperature curves gradually converge and eventually overlap. This occurs because the PCM temperature approaches the HTF temperature, which reduces the temperature difference and consequently lowers the heat transfer rate. Under these conditions, the effect of axial HTF temperature variation becomes negligible. Therefore, the constant-temperature boundary condition used in the parametric study provides a reasonable approximation for relatively short storage modules with sufficiently high HTF flow rates. This assumption may not remain valid for long heat exchangers or for systems with lower flow rates, where the HTF temperature drop along the flow direction could become significant. The flow rate was 0.4 lit/min in the experimental study. Hence, the present study focuses on the thermal behavior of a single storage module rather than the full performance of a long heat exchanger.

The temperature data corresponding to each thermocouple location were extracted and compared individually with the numerical predictions. The resulting comparison is now presented in Fig. 3d of the manuscript. The results depicted in this figure confirm a high level of consistency between the experimental outcomes and the simulations at all sensor locations, further confirming the validity of the developed model. The comparison with the reference experimental study shows that the error between the experimental measurements and the present numerical predictions is below 1% for all PCM temperature data reported in Fig. 3c and d. This confirms that the thermal field of the reference configuration, which directly governs the phase-change

process, is accurately captured. Moreover, the average error between the selected computational mode and the strict mode (i.e., finer mesh and smaller time step) is below 0.002 for both mesh and time-step sensitivity analyses. This indicates that the numerical uncertainty introduced by discretization is very small. It should be noted that this validation result corresponds to the reference configuration used for comparison with the experimental study. Modified geometries with different thermal resistances or smaller driving temperature differences may exhibit somewhat larger deviations. Therefore, the reported error can be considered as a lower-bound estimate of the numerical uncertainty of the model.

Further validation is provided in Fig. 3e, where the evolution of the melting front is compared with that of the reference work. The simulation closely follows the experimental plots throughout the charging process. The consistency in temperature rise, melting pattern, and the convergence of both datasets reinforce the reliability of the adopted approach. Based on these findings, it can be concluded that the chosen model, incorporating an $M_{rf}$ of $10^6$, meets the validation requirements and accurately predicts the melting dynamics of the PCM. Besides, the validation results confirm that neglecting axial temperature variations does not significantly affect the accuracy of predicted melting behavior under the operating conditions considered. Thus, the assumption of a constant wall temperature in a two-dimensional framework is considered appropriate and justified for the objectives of the present study, which focus on comparative performance analysis and geometric optimization rather than detailed axial HTF temperature evolution.

### 2.6. Mesh and time step independence

A mesh independence study is also performed to minimize discretization-related errors and to ensure that the obtained results remain unaffected by grid resolution. This step is particularly critical in PCM-based storage systems, where phase front tracking and steep temperature gradients occur near the heat transfer surfaces. The computational domain is discretized using a free quadrilateral mesh, which provides structured resolution around the cylindrical geometry. To improve accuracy in regions with high gradient intensity, a boundary layer mesh is incorporated, allowing for a more accurate capture of thermal and flow variations adjacent to the HTF tube walls. The generated mesh exhibits an average skewness of 0.33, which lies within the acceptable range for high-quality grids and ensures numerical stability. The influence of grid density on the predicted liquid fraction is illustrated in Fig. 4a. Up to the later stages of charging process, all three meshes produce nearly identical results. However, slight deviations appear in the later stages for the coarser mesh, whereas the intermediate and fine meshes exhibit excellent agreement. This convergence confirms that further refinement beyond 338,009 elements has a negligible impact on solution accuracy. Consequently, the intermediate mesh is adopted as the optimal choice, as it satisfies both reliability and computational efficiency. Since temporal resolution is also essential in phase change and natural convection problems, a time-step independence analysis is investigated, as depicted in Fig. 4b. The results in this diagram demonstrate that a time-step of 0.1 s is sufficient to capture the dynamic melting behavior without introducing numerical instabilities. The maximum mesh-induced error in liquid fraction for the system studied in the present work is below 1% for all liquid fraction values reported in Fig. 4. In absolute terms, the maximum difference in liquid fraction between the selected mode and the strict mode is less than 0.003, meaning that the average numerical error in liquid fraction is below 0.003. Therefore, although some designs show very close liquid fraction values, the differences reported in the manuscript are larger than the estimated numerical uncertainty. This confirms that the observed performance trends and comparisons between different geometrical configurations are meaningful and not artifacts of numerical error.

## 3. Machine learning techniques

Machine learning techniques, particularly artificial neural networks (ANNs), were employed in this study to develop a predictive framework for the melting behavior of the proposed TSD [55]. The utilization of ANN is motivated by its capacity to identify hidden patterns in nonlinear problems where multiple design parameters simultaneously influence thermal performance [56]. By generating such a predictive model, researchers can rapidly estimate system responses for new geometrical configurations, thereby reducing their reliance on repeated, time-consuming simulations [57]. The geometry of the storage chamber was characterized by three main design factors: the length of the straight bases ($L_{SB}$), the length of the tilted bases ($L_{TB}$), and the angle of the tilted bases ($\theta$). These variables were selected because they govern the distribution and alignment of the embedded tubes, thereby altering the available heat transfer surface area and ultimately the charging efficiency of the PCM. To systematically explore their influence, based on

**Table 4**
Coded variable levels for the three input parameters used in the ANN model.

| Variable | Variable levels | | |
|---|---|---|---|
| | −1 | 0 | +1 |
| $L_{SB}$ (mm) | 30 | 95 | 160 |
| $L_{TB}$ (mm) | 30 | 65 | 100 |
| $\theta$ (degree) | 60 | 90 | 120 |

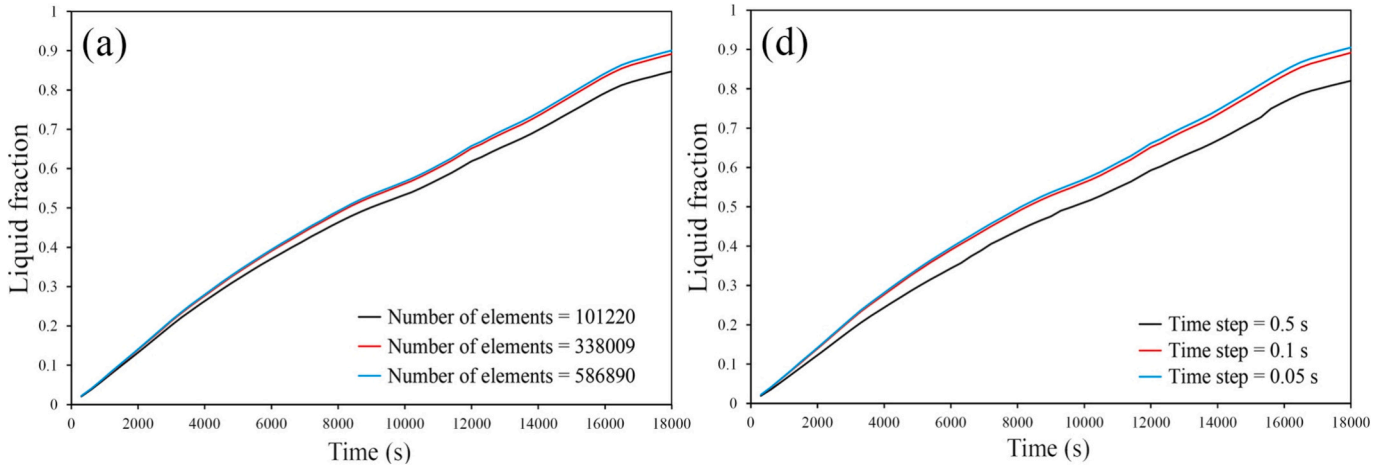


**Fig. 4.** The influence of (a) grid density and (b) time-step on the predicted liquid fraction for the system proposed in this study.

Table 4, each parameter was examined at three levels ($L_{SB}$ = 30, 95, 160 mm; $L_{TB}$ = 30, 65, 100 mm; $\theta$ = 60, 90, 120°). The full factorial design was employed, yielding $3^3 = 27$ unique system designs. This approach ensures that all possible interactions between the parameters are incorporated into the dataset, providing a comprehensive basis for training the network.

Since the input variables are expressed in different units (millimeters and degrees), the data were normalized before being entered into the network. Normalization prevents variables with larger numeric magnitudes from dominating the learning process, thereby improving convergence stability during training. The dataset was randomly assigned to three groups, with the majority used for training and the rest evenly divided between validation and testing. This arrangement is a standard practice in supervised learning, as it allows the network to learn from the majority of cases while still reserving sufficient samples to tune hyperparameters and evaluate predictive performance on unseen data. The ANN structure is illustrated in Fig. 5a. A feed-forward topology was selected, and the model was developed in MATLAB using the *feedforwardnet* function. The training process was conducted using the Levenberg–Marquardt algorithm, which provides rapid convergence for nonlinear regression problems and is widely regarded as one of the most effective algorithms for medium-sized networks. Nonlinear mapping was enabled in the hidden layers through the use of the hyperbolic tangent sigmoid (*tansig*) activation function, while a linear (*purelin*) function was employed in the output layer. The choice of a linear output function ensures that the predictions can take any real value, which is essential for the continuous nature of the target variables. The network was tasked with predicting the liquid fraction ($\varphi$) at two specific charging times, 2.5 h and 5 h, representing intermediate and near-complete melting states of the PCM. Including two outputs provides a broader perspective on the thermal response, rather than relying solely on the end-of-process data.

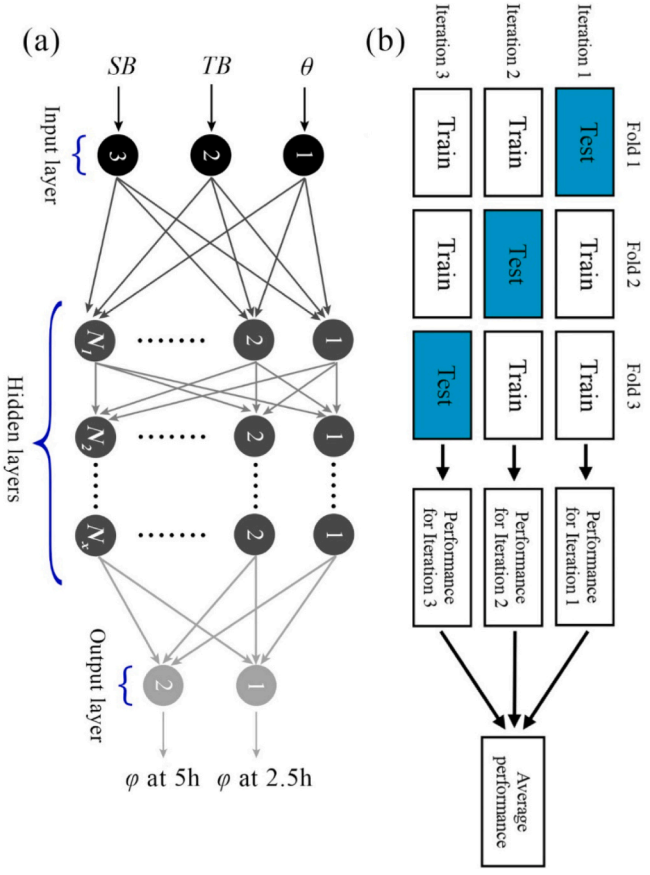


**Fig. 5.** (a) Schematic of the ANN with three inputs ($L_{SB}$, $L_{TB}$, and $\theta$) and two outputs ($\varphi$ at 2.5 h and 5 h). (b) Illustration of the k-fold cross-validation procedure employed to enhance generalization and minimize overfitting.

Model performance was assessed iteratively based on two complementary indices: $R^2$ and RMSE, as expressed in Eqs. (13) and (14). While $R^2$ quantifies how well the predictions replicate the trend of the actual data, RMSE measures the magnitude of the prediction errors. The simultaneous use of these metrics ensures that the model not only accurately follows the data trend but also precisely minimizes deviations. To further reduce the risk of overfitting and strengthen the network's generalization ability, a k-fold cross-validation scheme was implemented (Fig. 5b). In this approach, the dataset is divided into k folds, and the model is repeatedly trained and tested, with each fold serving as a test set once. The final performance is obtained by averaging the results across all folds, thus eliminating bias from a single arbitrary split.

$$R^2 = 1 - \frac{\sum_{i=1}^{m} \left(r_{num} - r_{pred}\right)^2}{\sum_{i=1}^{m} \left(r_{num} - \overline{r_{pred}}\right)^2} \tag{13}$$

$$RMSE = \sqrt{\frac{\sum_{i=1}^{m} \left(r_{pred} - r_{num}\right)^2}{m}} \tag{14}$$

## 4. Optimization procedure

While the ANN model provided a fast and reliable tool for predicting the melting behavior of the storage system, the next step was to identify the most effective geometric configuration of the bases. To achieve this, an optimization framework was developed using a genetic algorithm (GA). GA was selected due to its evolutionary search mechanism, which is well-suited for highly nonlinear and multi-dimensional problems such as PCM thermal storage [58]. Unlike gradient-based optimization, GA does not require explicit derivative information and is less likely to be trapped in local optima, making it an ideal candidate for this application [59]. The optimization was performed in two consecutive stages. In the first stage, a single-objective optimization was carried out. Two independent optimization runs were conducted: one to maximize the liquid fraction at 2.5 h, and another to maximize the liquid fraction at 5 h. Considering both objectives separately at this stage provides valuable insight into the trade-off between short-term and long-term melting performance. Specifically, enhancing the liquid fraction at the early stage (2.5 h) represents a system that can deliver faster charging, while maximizing the liquid fraction at 5 h targets complete utilization of the PCM storage capacity.

In the second stage, a multi-objective optimization was employed to maximize both liquid fraction values simultaneously. A Pareto front was generated, which highlights the balance between the two competing objectives. The multi-objective approach is crucial since it reflects practical scenarios in thermal energy storage where both rapid charging and high total energy absorption are desirable. Instead of converging toward a single solution, the Pareto front provides a set of optimal designs, enabling decision-makers to choose a configuration depending on whether priority is given to early-stage melting or overall storage completion. The GA parameters were carefully selected to ensure robust convergence and a diverse search of the design space. A population size of 1000 was adopted to maintain genetic diversity and reduce the risk of premature convergence. The maximum number of generations was set to 300, which is sufficient to allow the evolutionary process to refine candidate solutions without incurring excessive computational cost. An elite count of 50 was used, meaning that the top-performing solutions from each generation were preserved for the next iteration. Preserving elite individuals accelerates convergence by ensuring that the best designs are not lost during reproduction.

The mutation rate was set to 0.01, introducing controlled random

variations to prevent stagnation and maintain exploration of the solution space. A mutation rate that is too high would disrupt the convergence process, while one that is too low could lead to premature convergence; the chosen value strikes a balance between exploration and exploitation. The crossover rate was fixed at 0.8, reflecting the importance of recombining high-quality solutions to produce potentially superior offspring. Finally, the stochastic uniform selection method was applied. This selection strategy ensures a proportional, yet randomized choice of parents based on their fitness values, which prevents dominance of a small subset of solutions and maintains population diversity throughout the optimization process. Through this two-stage GA procedure, the study not only identifies the most effective design configurations for individual performance targets but also maps the trade-offs between conflicting objectives. This approach ensures that the final recommendations are both technically rigorous and practically flexible, supporting the design of more efficient PCM-based thermal energy storage systems.

## 5. Multi-criteria decision analysis through TOPSIS

Although the GA provides a set of optimal candidates through single- and multi-objective searches, a further decision-making tool is required to select the most appropriate configuration among them. For this purpose, the Technique for Order of Preference by Similarity to Ideal Solution (TOPSIS) was employed. TOPSIS is widely applied in engineering optimization problems because it simultaneously considers the closeness of each alternative to an ideal solution and its distance from an anti-ideal solution. This dual consideration ensures that the selected design is not only the best performer in terms of favorable attributes but also the farthest from undesirable outcomes. The procedure begins with the normalization of raw data values according to Eq. (15) [60]:

$$r_{ij} = \frac{x_{ij}}{\sqrt{\sum_{i=1}^{m} x_{ij}^2}} \tag{15}$$

Here, $x_{ij}$ represents the performance value of the $i^{th}$ design with respect to the $j^{th}$ criterion. Normalization is required because the original criteria (e.g., liquid fraction values at different charging times) may have different scales or units. By transforming them into dimensionless values, all criteria are given equal importance in making the decision without bias from magnitude differences. Once the data are normalized, they are weighted using Eq. (16) [61]:

$$v_{ij} = w_j \cdot r_{ij} \tag{16}$$

where $w_j$ is the weight assigned to the $j^{th}$ criterion. The use of weights allows the decision-maker to emphasize specific objectives more strongly than others. For example, if faster charging (liquid fraction at 2.5 h) is considered more critical than overall melting (at 5 h), a higher weight can be assigned accordingly. This step reflects practical engineering scenarios where priorities vary depending on application requirements. Eqs. (17) and (18) define the ideal and anti-ideal solutions, respectively [62]:

$$x_j^{ideal} = \max\{v_{ij}\} \tag{17}$$

$$x_j^{anti-ideal} = \min\{v_{ij}\} \tag{18}$$

The ideal solution represents the best performance values among all alternatives, while the anti-ideal solution reflects the worst. These definitions form the benchmark against which each candidate configuration is evaluated. Identifying these reference points is crucial because TOPSIS does not simply rank alternatives in isolation but measures how close each one is to the optimal and how far it is from the least desirable outcome. The distance of each design from the ideal and anti-ideal solutions is then computed using Eqs. (19) and (20) [63]:

$$D_i^{ideal} = \sqrt{\sum_{j=1}^{m} w_j \left(x_{ij} - x_j^{ideal}\right)^2} \tag{19}$$

$$D_i^{anti-ideal} = \sqrt{\sum_{j=1}^{m} w_j \left(x_{ij} - x_j^{anti-ideal}\right)^2} \tag{20}$$

These equations calculate Euclidean distances in the weighted normalized space. The rationale is that a truly desirable design needs to be near the ideal solution and away from the least desirable solution. Using weighted distances ensures that criteria with greater assigned importance have a stronger influence on the separation. Finally, the closeness coefficient ($CC$) is obtained from Eq. (21) [64]:

$$CC = \frac{D_i^{ideal}}{D_i^{ideal} + D_i^{anti-ideal}} \tag{21}$$

This coefficient provides a single scalar value ranging between 0 and 1. A value closer to 1 indicates that the design is very near the ideal solution and far from the anti-ideal, whereas a lower value suggests inferior performance. The advantage of this measure is that it integrates multiple criteria into a single ranking index while still preserving the influence of both best- and worst-case scenarios. Through this structured procedure, TOPSIS delivers a clear ranking of the candidate designs obtained from the optimization stage, enabling the selection of the most balanced configuration. This integration of GA-generated solutions with TOPSIS-based decision-making ensures that the final choice is both computationally rigorous and practically meaningful for real-world applications of PCM-based energy storage.

## 6. Results and discussion

### 6.1. Numerical evaluation of liquid fraction development

Table 5 provides the outcomes of 27 comprehensive simulations derived from a full factorial design. Each configuration combines three geometrical parameters of $L_{SB}$ (straight base length), $L_{TB}$ (tilted base length), and $\theta$ (tilted base angle) to study their influence on the liquid fraction evolution of the PCM at three time intervals: 1 h, 2.5 h, and 5 h. In addition to the design variables and the liquid fraction values, the following metrics are explicitly reported for each configuration:

- ➢ Surface area of the PCM box
- ➢ Maximum distance between HTF tubes
- ➢ Maximum distance between bases

These parameters directly reflect the effective heat transfer surface density and the largest conduction path within the PCM, which are key geometric factors governing the melting rate. Reporting these metrics allows the reader to better understand how changes in geometry influence the thermal performance, beyond the input parameters alone. The results capture the transient nature of melting, highlighting that different parameter combinations affect the dynamics of energy absorption and storage efficiency. To benchmark the role of base integration, a base-free design containing only HTF tubes was also included. Besides, three finned reference designs (Finned-design 15, Finned-design 50, and Finned-design 80), along with the base-free design, are included in Table 5. This provides a more meaningful engineering comparison between the proposed optimized base-integrated configurations and conventional fin-enhanced and non-enhanced designs. The surface area of the PCM box remains within a narrow range among the compared cases, ensuring that performance differences are primarily attributed to internal metal structure distribution and spacing, rather than trivial changes in PCM volume or container size. The maximum distance between tubes is identical for the base-free and finned-designs,

**Table 5**
Geometrical parameters of the 27 base-integrated designs and their corresponding surface area of PCM box, maximum distance between tubes, maximum distance between bases, and liquid fraction values at different charging durations (1 h, 2.5 h, and 5 h).

| Design number | Variables | | | Surface area of PCM box ($mm^3$) | Max distance between tubes (mm) | Max distance between bases (mm) | Liquid fraction at different times | | |
|---|---|---|---|---|---|---|---|---|---|
| | $L_{SB}$ (mm) | $L_{TB}$ (mm) | $\theta$ (degree) | | | | 1 h (3600 s) | 2.5 h (9000 s) | 5 h (18,000 s) |
| 1 | 160 | 100 | 120 | 155,947 | 184.423 | 231.288 | 0.252 | 0.528 | 0.892 |
| 2 | 160 | 100 | 90 | 155,947 | 184.423 | 174.409 | 0.256 | 0.562 | 0.887 |
| 3 | 160 | 65 | 120 | 157,347 | 254.425 | 231.288 | 0.250 | 0.539 | 0.895 |
| 4 | 160 | 65 | 90 | 157,347 | 254.425 | 174.409 | 0.251 | 0.563 | 0.878 |
| 5 | 160 | 30 | 120 | 158,747 | 324.423 | 231.288 | 0.253 | 0.536 | 0.906 |
| 6 | 160 | 30 | 90 | 158,747 | 324.423 | 174.409 | 0.254 | 0.551 | 0.866 |
| 7 | 160 | 100 | 60 | 155,947 | 184.423 | 231.288 | 0.261 | 0.572 | 0.823 |
| 8 | 160 | 65 | 60 | 157,347 | 254.423 | 231.288 | 0.255 | 0.564 | 0.814 |
| 9 | 160 | 30 | 60 | 158,747 | 324.423 | 231.288 | 0.253 | 0.557 | 0.807 |
| 10 | 95 | 30 | 60 | 161,347 | 324.423 | 231.288 | 0.236 | 0.524 | 0.770 |
| 11 | 95 | 65 | 60 | 159,947 | 254.423 | 231.288 | 0.242 | 0.532 | 0.801 |
| 12 | 95 | 100 | 60 | 158,547 | 194.423 | 231.288 | 0.245 | 0.544 | 0.789 |
| 13 | 95 | 30 | 90 | 161,347 | 324.423 | 174.409 | 0.238 | 0.543 | 0.810 |
| 14 | 95 | 30 | 120 | 161,347 | 324.423 | 231.287 | 0.236 | 0.517 | 0.748 |
| 15 | 95 | 65 | 90 | 159,947 | 254.423 | 174.409 | 0.237 | 0.563 | 0.854 |
| 16 | 95 | 65 | 120 | 159,947 | 254.423 | 231.288 | 0.238 | 0.525 | 0.761 |
| 17 | 95 | 100 | 90 | 158,547 | 194.423 | 174.409 | 0.243 | 0.546 | 0.861 |
| 18 | 95 | 100 | 120 | 158,547 | 194.423 | 231.288 | 0.242 | 0.544 | 0.775 |
| 19 | 30 | 30 | 60 | 163,947 | 324.423 | 231.288 | 0.221 | 0.447 | 0.713 |
| 20 | 30 | 65 | 60 | 162,547 | 324.423 | 231.288 | 0.234 | 0.479 | 0.725 |
| 21 | 30 | 100 | 60 | 161,147 | 324.423 | 231.288 | 0.242 | 0.530 | 0.769 |
| 22 | 30 | 30 | 90 | 163,947 | 324.423 | 174.409 | 0.222 | 0.468 | 0.704 |
| 23 | 30 | 30 | 120 | 163,947 | 324.423 | 231.288 | 0.218 | 0.435 | 0.596 |
| 24 | 30 | 65 | 90 | 162,547 | 324.423 | 174.409 | 0.228 | 0.504 | 0.772 |
| 25 | 30 | 65 | 120 | 162,547 | 324.423 | 231.288 | 0.226 | 0.476 | 0.668 |
| 26 | 30 | 100 | 90 | 161,147 | 324.423 | 174.409 | 0.235 | 0.533 | 0.813 |
| 27 | 30 | 100 | 120 | 161,147 | 324.423 | 231.288 | 0.232 | 0.511 | 0.730 |
| Finned-design 15 | | | | 165,441 | 173.471 | – | 0.161 | 0.320 | 0.435 |
| Finned-design 50 | | | | 163,378 | 173.471 | – | 0.236 | 0.471 | 0.650 |
| Finned-design 80 | | | | 161,611 | 173.471 | – | 0.265 | 0.517 | 0.776 |
| Base-free | | | | 166,322 | 173.471 | – | 0.111 | 0.250 | 0.368 |

while the maximum distance between tubes is substantially increased in the optimized designs due to the presence and strategic orientation of the bases.

During the first hour, the liquid fraction values of all 27 designs remain within a narrow range, clustering around 0.25. This indicates that in the early stages, heat conduction dominates, and geometric distinctions have not yet introduced marked differences in melting performance. By contrast, the base-free storage only reaches a liquid fraction of 0.111. This means that even the least effective base-integrated design achieves more than 126% higher melting progress than the base-free design within this initial period. Such an improvement demonstrates the crucial role of bases in accelerating the onset of melting, as they enhance conductive and convective heat distribution from the tubes to the PCM. A similar trend is observed when comparing the base-integrated designs with the finned reference configurations. Among the three finned designs, Finned-design 80 (with the longest fins) exhibits the best performance at 1 h, reaching a liquid fraction of 0.265, whereas Finned-design 50 and Finned-design 15 reach only 0.236 and 0.161, respectively. This confirms that increasing fin penetration enhances early-stage heat transfer; however, the optimized base-integrated designs still outperform the finned configurations. Compared to Finned-design 80, the base-integrated configurations show only about a 1.5% lower melting progress at 1 h, indicating nearly equivalent early-stage thermal performance. In contrast, the finned configurations with shorter fins show clearly weaker performance. Specifically, compared with Finned-design 15 (liquid fraction = 0.161), the base-integrated designs exhibit about 55% higher melting progress within the first hour. Even relative to Finned-design 50 (liquid fraction = 0.236), the base-integrated configurations provide an improvement of approximately 6%.

As the melting progresses to 2.5 h, disparities between designs become increasingly evident. The highest liquid fraction (0.572 in Design 7) nearly doubles the lowest (0.435 in Design 23). Compared to the base-free system (0.250), the best-performing case achieves a liquid fraction that is approximately 129% greater. At this stage, convection becomes increasingly influential, and the geometric configuration of bases dictates how effectively the liquid PCM circulates and redistributes heat. The pronounced gap between the highest and lowest values confirms that optimal base dimensions and inclination angles are critical in sustaining efficient melting during mid-duration solar charging. A clear advantage of the proposed optimal designs over conventional finned configurations can also be observed: at 2.5 h, Design 7 reaches a liquid fraction of 0.572, while Finned-design 80 reaches 0.517. This corresponds to a relative improvement of 10.6%, indicating that the optimized base configuration achieves about 10.6% higher liquid fraction than the best-performing finned reference design at this intermediate charging time.

By the end of the 5 h, the differences become even more striking. The maximum liquid fraction, recorded for Design 5 at 0.906, far exceeds the minimum (0.596 in Design 23). In comparison to the base-free design, which achieves only 0.368, the optimal design demonstrates an improvement of approximately 146%. This outcome emphasizes the cumulative effect of integrating properly dimensioned bases. While the base-free unit stagnates at limited melting due to weak conduction paths and poor convective circulation, base-supported systems maintain efficient melting propagation throughout the storage medium. The results reinforce the notion that, under realistic solar irradiation durations of about 4–6 h, the geometrical optimization of bases plays a decisive role in enhancing the storage capacity of PCM-based systems. Hence, the numerical dataset in Table 5 not only establishes the performance differences between designs but also highlights the inadequacy of base-free configurations for practical thermal energy storage. At 5 h, Finned-design 80 reaches a liquid fraction of 0.776. The corresponding improvement is 16.8%, demonstrating that Design 5 provides

approximately 16.8% higher melting fraction than the finned reference case at longer charging times. These comparisons confirm that, even when benchmarked against engineering designs with extended heat transfer surfaces (fins), the proposed base-integrated optimal configurations provide measurable and meaningful performance gains, not merely improvements over a simplistic base-free geometry.

From the complete set of 27 configurations, six representative cases were extracted to highlight the influence of the geometric parameters on thermal storage performance. These designs were chosen strategically: Design 1 corresponds to the maximum values of all parameters ($L_{SB}$ = 160 mm, $L_{TB}$ = 100 mm, $\theta$ = 120°), Design 15 represents mid-range parameter settings ($L_{SB}$ = 95 mm, $L_{TB}$ = 65 mm, $\theta$ = 90°), and Design 19 embodies the minimum parameter values ($L_{SB}$ = 30 mm, $L_{TB}$ = 30 mm, $\theta$ = 60°). To provide contrast, Designs 5, 7, and 27 modify only a single parameter relative to Design 1; specifically, reducing $L_{TB}$, $\theta$, or $L_{SB}$ to their minimum value, respectively. For reference, the base-free system, lacking structural bases, was also included. The results in Fig. 6a demonstrate that the liquid fraction of all six designs substantially exceeds that of the base-free system, underscoring the critical role of bases in accelerating the melting process. The gap between base-free and base-integrated systems becomes progressively larger as melting advances, reflecting how enhanced conduction and guided convection within the PCM expedite phase change. Interestingly, despite all six designs being superior to the base-free case, they do not perform identically. The curves reveal that Design 7 initially achieves the highest melting rate, likely due to its smaller $\theta$ value that promotes more effective thermal

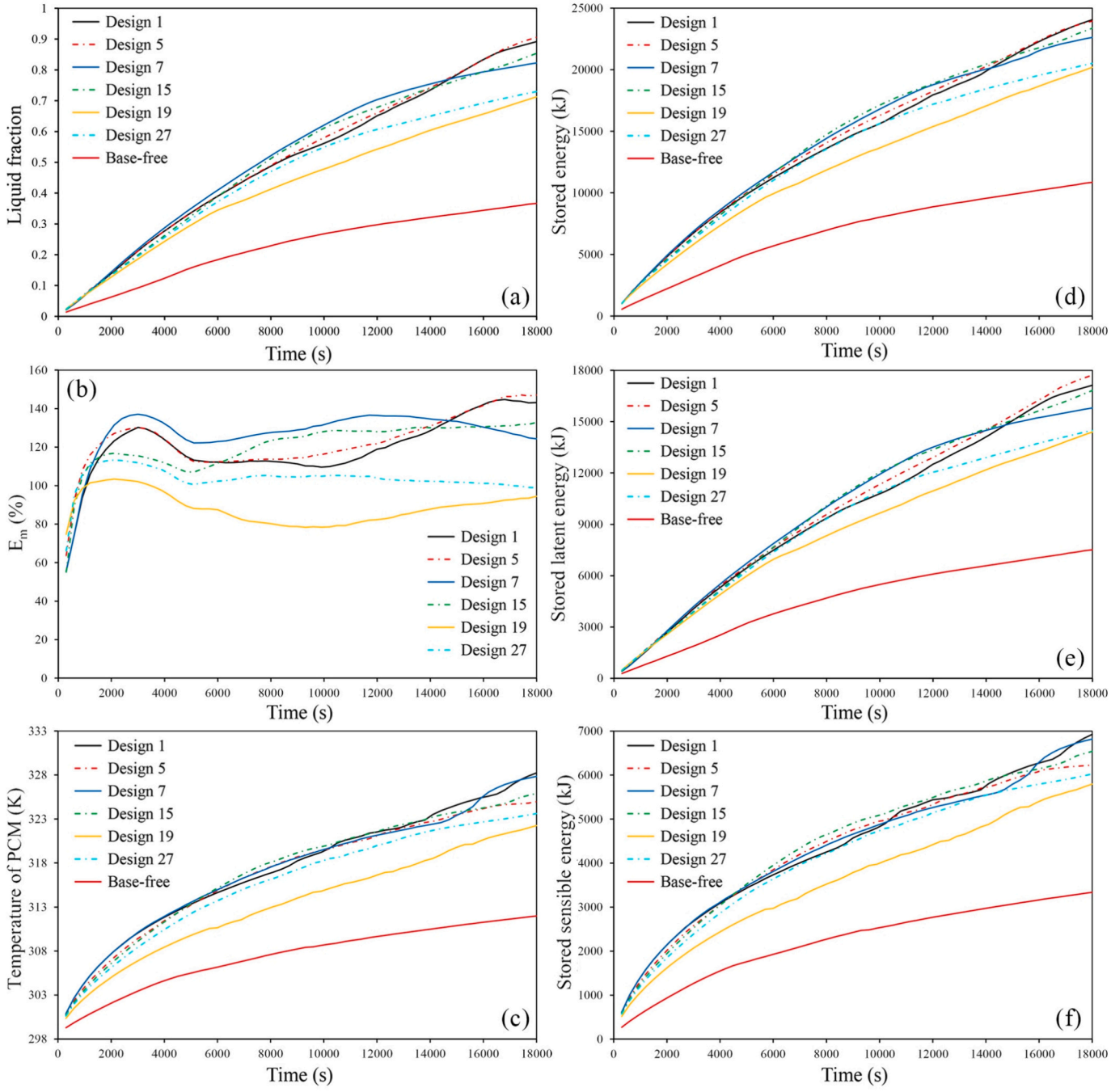


**Fig. 6.** Time-dependent variations of melting and energy absorption metrics for six selected base-integrated configurations (Designs 1, 5, 7, 15, 19, and 27) compared with the base-free system.

pathways.

However, as melting progresses, Designs 1 and 5 surpass Design 7, with Design 5 ultimately delivering the best performance. This improvement arises from its minimum tilted base length ($L_{TB}$). Although reducing $L_{TB}$ decreases the overall surface area available for heat transfer, it provides a more favorable geometric arrangement that enhances long-term melting performance. In this configuration, the tubes are positioned closer to the outer walls of the PCM box, thereby activating convective circulation patterns in regions that would otherwise remain underutilized. This strategic distribution of thermal influence enables the delivery of heat more uniformly across the domain, thereby improving the overall melting capacity. Hence, the study highlights that longer bases, despite offering greater surface areas, do not always guarantee better outcomes, and the geometric positioning of heat transfer structures proves to be equally, if not more, important.

At the opposite end of the spectrum, Design 19 represents the weakest performance among all cases. This deficiency stems from two primary reasons: first, the reduction in surface area due to minimal base dimensions restricts the conductive pathways available for heat entry; second, the arrangement of the tubes primarily toward the sides of the PCM box leaves the central region poorly served. As a result, large pockets of PCM remain insufficiently activated, leading to slower melting and lower energy absorption. Design 1 offers another instructive case. While its configuration concentrates the tubes toward the central area of the PCM domain, potentially reducing the uniformity of heat distribution, this drawback is compensated by its relatively larger base surfaces. The increased heat transfer area partially balances the shortcomings of tube positioning, resulting in a performance that remains competitive with the leading designs.

These trends are well illustrated in Fig. 6b, which depicts the improvement percentages of the selected designs relative to the base-free reference case. For example, Design 5 shows an improvement of approximately 130.2% over the base-free design at 300 s, clearly indicating its superior capability in accelerating the early stages of melting. This advantage remains unchanged over time. In fact, even near the end of the melting process, at 17400 s, the improvement margin for Design 5 rises to about 147.2%, emphasizing that the gap between base-integrated and base-free systems persists and even widens. This is because the base-free design remains significantly constrained in its ability to promote effective conduction and natural convection, whereas the base-integrated systems continue to benefit from their optimized geometric features. Notably, the curves reveal no tendency for the improvements to converge in the later stages, confirming that base integration not only accelerates early melting but also sustains its advantage throughout the full charging duration.

The thermal response of the system can be further understood through the average PCM temperature evolution presented in Fig. 6c. Among the selected designs, Design 1 achieves the most favorable temperature rise, a direct consequence of its relatively larger base surface area, which enhances heat conduction and promotes uniform thermal distribution. This broader surface contact enables the PCM to absorb heat more rapidly and consistently, resulting in a more uniform temperature field. Design 7 follows closely, exhibiting a comparable trend, particularly in the mid-to-late stages of melting. However, Design 5, despite being superior in terms of liquid fraction, shows a weaker ability to elevate PCM temperature. This discrepancy highlights the complex interplay between geometric arrangement and heat storage mechanisms: while shortened bases bring the tubes closer to the box walls and accelerate melting, they do not necessarily guarantee an equally rapid or uniform increase in PCM temperature. A distinctive feature in Fig. 6c is the presence of a plateau region, most noticeable between approximately 3000 and 15,000 s. The temperature curve does not exhibit a perfectly flat plateau. Instead, what is observed is a distinct reduction in the slope of the temperature–time curve during the melting period. This decrease in slope indicates that the rate of temperature rise slows down when phase change becomes dominant. Physically, this corresponds to the stage where a considerable portion of the supplied thermal energy is consumed as latent heat rather than contributing to further sensible temperature increase. Once most of the PCM has melted, the slope increases again, reflecting the resumption of predominantly sensible heating. It is also important to note that Fig. 6c reports the volume-averaged PCM temperature rather than the temperature at a single point. In different regions of the PCM domain, melting and sensible heating may occur simultaneously. As a result, when averaged over the entire PCM volume, the classical “flat” plateau typically observed in local temperature histories is smoothed into a gradual change in slope.

Moving to the total stored energy results in Fig. 6d, where Design 1 once again demonstrates the highest energy storage, aligning with its superior PCM temperature rise and competitive liquid fraction values. Yet, a noteworthy finding emerges when comparing Design 5 and Design 1: despite Design 5's weaker temperature rise, its stored energy nearly matches that of Design 1. This apparent contradiction is resolved by considering the distribution of sensible and latent storage. Because Design 5 has shorter bases, more PCM volume is available in the system. As a result, even though its sensible energy storage is reduced due to the lower average PCM temperature, the additional PCM mass allows it to absorb more latent heat. The balance between these two contributions enables Design 5 to achieve stored energy values equivalent to those of Design 1. The superiority of base-integrated designs over the base-free reference is striking across all subplots. For instance, by the end of the charging cycle, Design 1 stores approximately 121.7% more total energy compared to the base-free system, and Design 5 shows nearly 120.6% improvement.

This behavior becomes clearer when examining Fig. 6e and f, which separate latent and sensible energy components. Fig. 6e shows that Design 5 dominates in terms of latent energy storage, outperforming all other designs. This advantage directly results from the larger PCM volume available to undergo phase transition, combined with its high liquid fraction. In contrast, Fig. 6f indicates that Design 1 achieves the highest sensible energy storage, reflecting its ability to raise the PCM temperature more effectively than the others. These two outcomes reinforce the idea that system performance is governed by a trade-off between sensible and latent contributions, which are strongly influenced by base geometry. In latent storage alone, Design 5 achieves around 135.8% betterment compared to base-free, underscoring the importance of maximizing PCM volume and phase-change potential. On the sensible side, Design 1 provides a roughly 107.5% improvement over the base-free design, driven by its enhanced temperature rise. These percentages emphasize that while the optimal geometry can vary depending on whether latent or sensible contributions are prioritized, all integrated bases decisively outperform the base-free configuration.

### 6.2. *Development of predictive models using ANN*

The performance of an ANN is not merely a matter of feeding data into a black box; the network's structure itself profoundly shapes it. The number of layers, the number of neurons in each layer, and the choice of activation functions collectively determine how well the model can extract patterns and generalize unseen cases. In this study, different ANN architectures were systematically examined, beginning from the most elementary configuration (a single hidden layer with two neurons) and progressively extending toward more complex networks with three hidden layers and up to ten neurons in each. The primary objective was to strike a balance between model expressiveness and the risk of overfitting, ensuring that the final architecture could achieve both high accuracy and generalization capability. After extensive testing, the architecture that consistently provided the best trade-off was a 3–8–2 configuration, which was sufficient to capture the nonlinear relationships between the geometric parameters of the system and the liquid fractions at both 2.5 h and 5 h. This architecture demonstrated that sometimes a carefully chosen, moderately complex network can outperform unnecessarily deep models, emphasizing that elegance in

ANN design often lies in restraint. The complete mathematical description of the ANN requires the specification of its internal parameters, including weights and biases, that govern the transformation of inputs into outputs. These values, obtained after the optimization process using the Levenberg–Marquardt algorithm, are reported in Table 6. They constitute the backbone of the prediction model, ensuring reproducibility for future researchers who may wish to apply or extend this trained network.

To assess the predictive reliability of the developed ANN, performance metrics such as $R^2$ and RMSE were calculated. The outcomes, summarized in Table 7, reveal remarkable accuracy, with the model achieving $R^2 = 0.985$ for the liquid fraction at 2.5 h and $R^2 = 0.981$ at 5 h. Correspondingly, the RMSE values were as low as 0.004 and 0.010, respectively. These results demonstrate the network's precision in reproducing simulation data, with deviations that are practically negligible for engineering applications. In essence, the ANN does not merely interpolate the data; it constructs a predictive framework that faithfully mirrors the physics-driven numerical simulations. The high $R^2$ values signify an almost perfect correlation between predicted and actual results, while the low RMSE values confirm that the residual errors are insignificant. Such outcomes demonstrate the robustness of the network, which can now serve as a ready-to-use surrogate model for rapid prediction of melting behavior in future designs, dramatically reducing the computational cost of repeated simulations.

The reliability of the developed ANN prediction model is also demonstrated in Fig. 7a and b, where the predicted liquid fraction values are plotted against those obtained from numerical simulations. The results exhibit an almost perfect alignment with the 45° line, confirming that the model not only follows the general trend but also captures the acceptable variations of the data with remarkable precision. The clustering of points tightly around the line indicates that discrepancies between predicted and actual values are minimal, and no systematic deviation is observed across the range of values. This outcome highlights the effectiveness of the adopted ANN structure, which is capable of replicating the complex, nonlinear relationships inherent in phase change heat transfer systems. To further ensure that the model is not overfit to a particular partitioning of the dataset, a k-fold cross-validation procedure was employed. The 27-case dataset was split into three folds, where each cycle employed 18 cases for training and 9 for testing. The procedure was repeated three times, ensuring that each case served once as a validation instance. The consistent accuracy across all folds provided compelling evidence that the choice of training and testing subsets does not bias the ANN. In practical terms, this means the model's predictive ability is stable and does not deteriorate when exposed to unseen data. The statistical uncertainty of the ANN predictions is summarized in Table 8, where the mean values, standard deviations, 95% coverage intervals, and 95% confidence intervals of the predicted liquid fractions at 2.5 h and 5 h are provided. As shown in Table 8, the ANN model exhibits low dispersion in its predictions, reflected by the small standard deviations (0.025 for $\varphi_{2.5h}$ and 0.051 for $\varphi_{5h}$). The 95% coverage intervals indicate that most of the predicted values are tightly distributed around the mean, confirming the stability of the trained network over the input design space. Moreover, the narrow 95% confidence intervals of the mean predictions (0.538–0.539 for $\varphi_{2.5h}$ and 0.820–0.821 for $\varphi_{5h}$) demonstrate the high reliability and statistical robustness of the ANN model in estimating the average melting performance. These results confirm that the ANN model not only provides accurate predictions (as discussed through $R^2$ and error metrics) but also exhibits low predictive uncertainty, strengthening confidence in its application for optimization and design exploration. Besides, to quantify the propagation of uncertainties into the predicted melting performance, a Monte Carlo simulation was performed. The probability density distributions of the predicted liquid fractions are presented in Fig. 7c and d. Fig. 7c illustrates the probability density of $\varphi_{2.5h}$ obtained from the Monte Carlo samples. The distribution exhibits a unimodal shape with a relatively narrow spread, indicating that the predicted melting fraction at 2.5 h is only weakly sensitive to moderate uncertainties in the input parameters. The concentration of probability mass around the mean value confirms that the short-term charging performance of the system is robust against plausible variations in material properties and operating conditions. Similarly, Fig. 7d shows the probability density distribution of $\varphi_{5h}$. Compared with $\varphi_{2.5h}$, the distribution is slightly broader, reflecting the accumulation of uncertainty effects over longer charging times. Nevertheless, the distribution remains compact and unimodal, demonstrating that the long-term melting performance is also stable and predictable despite uncertainties in the input parameters. This behavior is consistent with the uncertainty ranges reported in Table 8, further confirming the reliability of the ANN model for uncertainty propagation and design assessment.

**Table 7**
Performance evaluation of the ANN prediction model using $R^2$ and RMSE.

| Loss function | ANN model | |
|---|---|---|
| | $\varphi_{2.5h}$ | $\varphi_{5h}$ |
| $R^2$ | 0.985 | 0.981 |
| RMSE | 0.004 | 0.010 |

Figs. 7e–7j provide the three-dimensional response surfaces of the liquid fraction at 2.5 h and 5 h as a function of the geometric parameters. These surfaces not only highlight the nonlinear interactions among the design variables but also reveal which parameters play the most decisive roles in accelerating the melting process. In Fig. 7e, it is evident that enlarging the $L_{TB}$ generally increases the liquid fraction at 2.5 h. However, the impact of $L_{TB}$ is not uniform: at smaller $L_{SB}$ values, the sensitivity of the liquid fraction to $L_{TB}$ is much stronger, whereas at larger $L_{SB}$ values, the influence of $L_{TB}$ diminishes. On the other hand, expanding the $L_{SB}$ itself is consistently favorable for enhancing the liquid fraction, though the effect is more pronounced when $L_{TB}$ is small. This asymmetry suggests that $L_{SB}$ and $L_{TB}$ reinforce each other at lower values, but once one parameter reaches a sufficiently high magnitude, the marginal contribution of the other diminishes.

In Fig. 7f, the role of the angle $\theta$ introduces a more complex trend.

**Table 6**
Optimized weights and biases defining the final ANN architecture (3–8–2) for predicting liquid fraction at 2.5 h and 5 h.

| Hidden layer | | | | Output layer | | | |
|---|---|---|---|---|---|---|---|
| Weights (8 × 3) | | | Biases (8 × 1) | Model of $\varphi_{2.5h}$ | | Model of $\varphi_{5h}$ | |
| | | | | $Weights^T$ (8 × 1) | Bias (1 × 1) | $Weights^T$ (8 × 1) | Biass (1 × 1) |
| 0.882 | −0.415 | 3.038 | 2.532 | 0.174 | −0.445 | 0.326 | −0.455 |
| 1.617 | −0.287 | 2.362 | −2.092 | −0.237 | | 0.140 | |
| 0.156 | 1.295 | −1.758 | −2.523 | 0.202 | | 0.080 | |
| −2.388 | 0.316 | 2.043 | −0.579 | 0.033 | | −0.389 | |
| 0.018 | 1.419 | 2.501 | 0.870 | −0.005 | | 0.128 | |
| −2.892 | 0.750 | −0.886 | −0.833 | −0.242 | | 0.207 | |
| −2.190 | −1.816 | −0.104 | −2.299 | −0.508 | | −0.268 | |
| −1.210 | −0.226 | 2.085 | −3.066 | −0.402 | | −0.589 | |

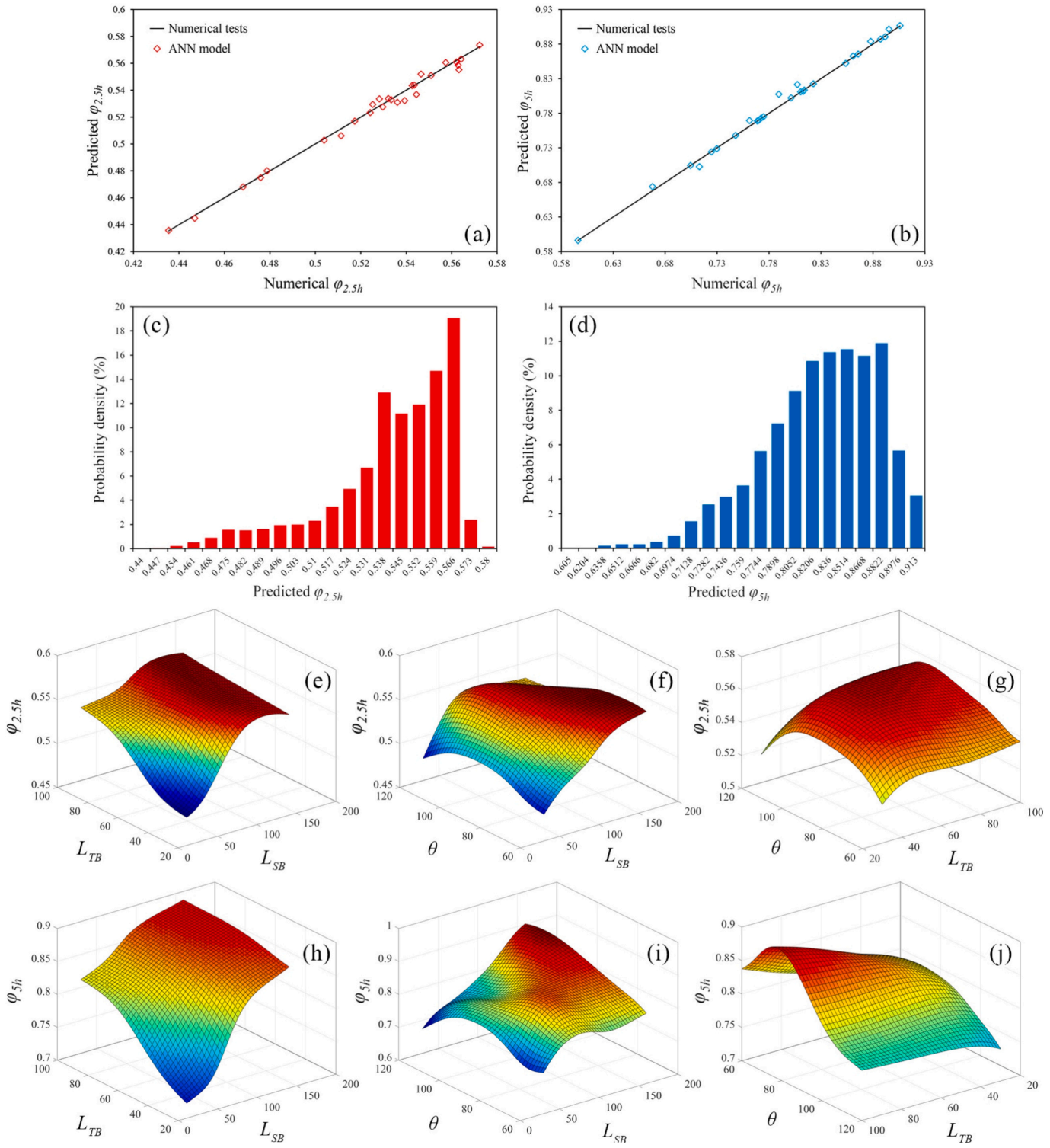


**Fig. 7.** Validation and response surface representation of the ANN prediction model. (a) Parity plot comparing numerical and ANN-predicted liquid fraction at 2.5 h. (b) Parity plot comparing numerical and ANN-predicted liquid fraction at 5 h. Probability density distribution of the predicted liquid fraction at (c) 2.5 h and (d) 5 h obtained from Monte Carlo uncertainty analysis. (e–g) 3D response surfaces for liquid fraction at 2.5 h as a function of geometric parameters. (h–j) 3D response surfaces for liquid fraction at 5 h as a function of geometric parameters.

Initially, increasing $\theta$ enhances the liquid fraction at 2.5 h, indicating that moderate angular widening facilitates improved heat transfer and faster PCM melting. Yet beyond a threshold, further increasing $\theta$ reduces the liquid fraction, likely due to less efficient distribution of thermal energy at large angles. Meanwhile, the effect of $L_{SB}$ varies depending on $\theta$. At smaller angles, the behavior of $L_{SB}$ is straightforward; larger $L_{SB}$ values correspond to higher liquid fractions. At larger $\theta$ values, however, $L_{SB}$ initially improves the melting fraction; however, after a certain point, excessive $L_{SB}$ appears to reduce efficiency, indicating that geometric trade-offs exist between $\theta$ and $L_{SB}$. Fig. 7g illustrates that the combined influence of $L_{TB}$ and $\theta$ on the liquid fraction at 2.5 h is comparatively weaker. The color gradients are subtle, indicating minor

**Table 8**
Statistical uncertainty analysis of ANN predictions for liquid fraction at 2.5 h and 5 h.

| Model | Mean | Standard deviation | 95% Coverage interval | | 95% Confidence interval | |
|---|---|---|---|---|---|---|
| | | | Lower bound | Upper bound | Lower bound | Upper bound |
| $\varphi_{2.5h}$ | 0.538 | 0.025 | 0.472 | 0.566 | 0.538 | 0.539 |
| $\varphi_{5h}$ | 0.821 | 0.051 | 0.706 | 0.900 | 0.820 | 0.821 |

variations. This observation confirms that, at this intermediate stage of melting, $L_{SB}$ remains the dominant driver, while the effects of $L_{TB}$ and $\theta$ are less critical.

Moving to the 5 h mark, Fig. 7h displays a trend similar to Fig. 7e: the enlargement of $L_{TB}$ increases the liquid fraction, with its effect amplified at lower $L_{SB}$ values. $L_{SB}$ again demonstrates a robust positive impact, particularly when $L_{TB}$ is small. Thus, the interaction between $L_{SB}$ and $L_{TB}$ is consistent across both early and later stages of melting. In Fig. 7i, the interplay between $\theta$ and $L_{SB}$ becomes more significant than at 2.5 h. At low $L_{SB}$ values, the variation of $\theta$ shows a peak behavior, first increasing and then decreasing the liquid fraction. At high $L_{SB}$ values, however, increasing $\theta$ steadily enhances the liquid fraction, and the effect becomes stronger as $L_{SB}$ increases. This indicates that the influence of $\theta$ depends heavily on the extent of $L_{SB}$, and at higher $L_{SB}$ values, the positive synergy between the two parameters substantially improves melting performance. Fig. 7j illustrates the combined effect of $L_{TB}$ and $\theta$ on the liquid fraction at 5 h. Although the gradient is still milder compared to other surfaces, it is more pronounced than in Fig. 7g. This suggests that the role of $L_{TB}$ and $\theta$ becomes more meaningful in later stages of melting, where the solid–liquid interface is more advanced and heat transfer patterns are different. Taken together, the surfaces reveal that $L_{SB}$ is the most decisive parameter, consistently influencing the liquid fraction across both time intervals, while $L_{TB}$ and $\theta$ exhibit more context-dependent effects. At 2.5 h, $L_{SB}$ dominates, but by 5 h, the interactions between $L_{SB}$ and $\theta$ gain greater importance, underlining the nonlinear and time-dependent nature of the system's thermal response.

### 6.3. Optimization of geometric parameters using GA

While the three-dimensional response surfaces presented earlier provide valuable qualitative insights into how each geometric parameter ($L_{SB}$, $L_{TB}$, and $\boldsymbol{\theta}$) influences the melting behavior of the system, these surfaces can only approximate the trends. To obtain precise optimal parameter values, a systematic optimization technique is essential. In this work, a GA was employed to rigorously search the parameter space and determine the most efficient configurations. In the first step of the GA process, single-objective optimization was performed. Two distinct objectives were set: (1) Maximization of the liquid fraction at 2.5 h ($\varphi_{2.5h}$), and (2) Maximization of the liquid fraction at 5 h ($\varphi_{5h}$). The GA algorithm yielded two optimal geometric configurations: Half-Melting Optimal (HMO) for the first objective and Full-Melting Optimal (FMO) for the second.

The corresponding optimized values of $L_{SB}$, $L_{TB}$, and $\boldsymbol{\theta}$ for these two configurations are summarized in Table 9. HMO corresponds to $L_{SB}$ = 160 mm, $L_{TB}$ = 100 mm, and $\boldsymbol{\theta}$ = 67.050°, while FMO corresponds to $L_{SB}$ = 160 mm, $L_{TB}$ = 44.105 mm, and $\boldsymbol{\theta}$ = 110.820°. The accuracy of the optimization results can be assessed by comparing the predicted liquid fraction values (from the ANN model) with those obtained by numerical simulations for both HMO and FMO, as shown in Table 10. The differences between predicted and numerical values are consistently small, confirming the high precision and reliability of the prediction model. For example, for FMO at $\varphi_{5h}$, the predicted value (0.913) matches the numerical result (0.913) exactly. Similarly, for HMO at $\varphi_{2.5h}$, the predicted and numerical values are 0.576 and 0.575, respectively. These close agreements strongly validate the predictive framework used for guiding the optimization process.

**Table 9**
Optimized geometric parameters obtained using the GA for HMO, FMO, BMO, and Design 5.

| Optimized response | Symbol of design | Design variables | | |
|---|---|---|---|---|
| | | $L_{SB}$ (mm) | $L_{TB}$ (mm) | $\theta$ (degree) |
| $\varphi_{2.5h}$ | HMO | 160 | 100 | 67.050 |
| $\varphi_{5h}$ | FMO | 160 | 44.105 | 110.820 |
| $\varphi_{2.5h}$ and $\varphi_{5h}$ (TOPSIS-selected) | BMO | 160 | 100 | 76.751 |
| Design 5 (Optimal in Table 5) | | 160 | 30 | 120 |

**Table 10**
Comparison between predicted and numerical liquid fraction results for HMO, FMO, BMO, and Design 5.

| Symbol of design | Predicted results | | Numerical test results | |
|---|---|---|---|---|
| | $\varphi_{2.5h}$ | $\varphi_{5h}$ | $\varphi_{2.5h}$ | $\varphi_{5h}$ |
| HMO | 0.576 | 0.861 | 0.575 | 0.847 |
| FMO | 0.534 | 0.913 | 0.551 | 0.913 |
| BMO | 0.572 | 0.881 | 0.563 | 0.873 |
| Design 5 (Optimal in Table 5) | – | – | 0.536 | 0.906 |

Further insights emerge when comparing the total stored energy for the two optimal designs. At 2.5 h, HMO and FMO stored 15,516 kJ and 15,707 kJ, respectively, while at 5 h, the total stored energies were 23,236 kJ and 24,359 kJ. Interestingly, despite HMO achieving a higher liquid fraction at 2.5 h, its total stored energy is lower than that of FMO at both time intervals. The sensible energy contribution can explain this. The shorter tilted base length in FMO allows for a larger PCM volume, which in turn leads to higher sensible heat storage. Consequently, although HMO has a slightly faster melting rate in the early period, FMO ultimately surpasses it in total energy storage due to its greater PCM capacity and enhanced sensible energy absorption. This outcome highlights a necessary design trade-off: maximizing the liquid fraction does not always result in the highest total energy storage, as both sensible and latent contributions must be considered simultaneously. The GA-based optimization effectively captures these subtleties, identifying configurations that balance melting rate, PCM volume, and heat transfer characteristics.

While single-objective optimization provides valuable insight into extreme performance conditions, such as achieving the highest liquid fraction at a specific time, it inherently focuses on only one performance target at a time. However, in practical thermal storage applications, a balanced performance is often more desirable than excelling in just one criterion. For example, a design that melts PCM rapidly in the early charging stage may not necessarily maintain superior energy storage after prolonged operation. Conversely, a design optimized for late-stage performance may compromise initial melting rates. Therefore, incorporating a multi-objective optimization approach is crucial to identify compromise solutions that simultaneously offer strong performance across different operating durations. Fig. 8 illustrates the Pareto front obtained from the second step of GA optimization, where both $\varphi_{2.5h}$ and $\varphi_{5h}$ were considered as objective functions simultaneously. The blue points represent random design configurations distributed throughout the design space, while the red points form the Pareto front, representing non-dominated optimal solutions. Each Pareto point signifies a design for which any improvement in one objective would necessarily lead to deterioration in the other.

As expected, the previously obtained HMO and FMO designs appear at the two extremities of the Pareto front, HMO corresponding to maximum early-stage melting and FMO to maximum long-term melting. However, for practical operation, neither extreme may represent the

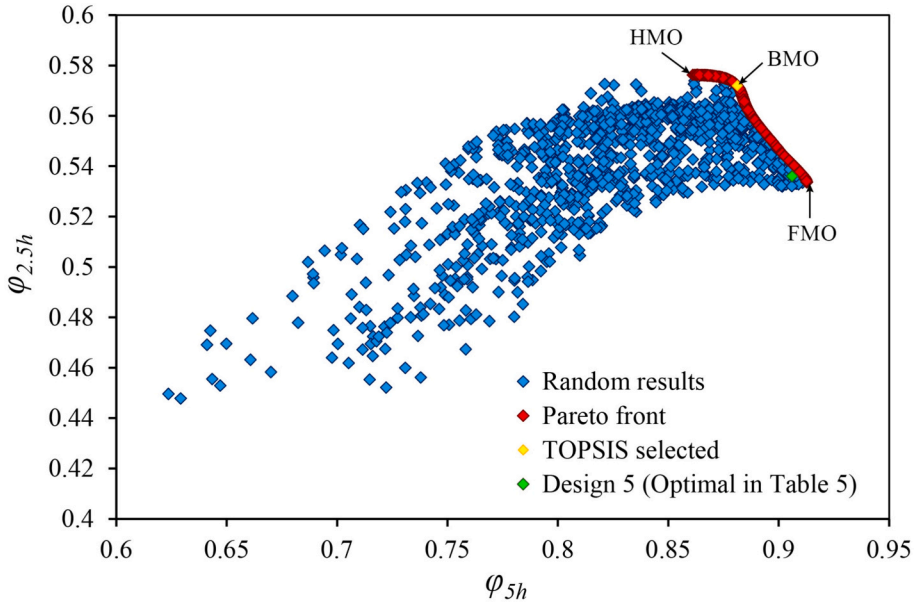


**Fig. 8.** Pareto front obtained from multi-objective GA optimization, considering $\varphi_{2.5h}$ and $\varphi_{5h}$ simultaneously. The TOPSIS method identifies BMO as the best compromise solution between early and long-term melting performance.

best overall choice. To address this, the TOPSIS method was applied to select an ideal solution from the Pareto front. TOPSIS evaluates each Pareto solution based on its CC value. The TOPSIS-selected design, named Balanced-Melting Optimal (BMO), has a closeness coefficient of 0.667, indicating its strong proximity to the ideal solution. Structurally, based on Table 9, BMO corresponds to $L_{SB} = 160$ mm, $L_{TB} = 100$ mm, and $\theta = 76.751°$. The predicted liquid fractions at 2.5 and 5 h for BMO are 0.572 and 0.881, respectively, falling between the values of HMO and FMO, as expected for a balanced design. Additionally, the total stored energy of BMO reaches 15,500 kJ after 2.5 h and 23,810 kJ after 5 h, reflecting a well-balanced performance across both time intervals. The results highlight the power of multi-objective optimization in identifying solutions that single-objective strategies might overlook. By considering multiple performance goals simultaneously, the Pareto front provides a spectrum of optimal trade-offs, and methods like TOPSIS allow designers to select the most suitable configuration for specific operational priorities. The best parametric design among the 27 simulated cases (Design 5), which exhibits the highest liquid fraction at 5 h, is explicitly included in Tables 9 and 10 and Fig. 8 for direct comparison with the ANN-optimized designs. From Table 10, it is observed that the ANN-derived FMO reaches a liquid fraction of 0.913 at 5 h, while Design 5 reaches 0.906, corresponding to an improvement of approximately 0.77%. It is true that this improvement is numerically small. However, it is achieved solely by modifying the geometric parameters of the bases (length and angle), without introducing additional material, increasing system volume, or adding manufacturing complexity. From an engineering and manufacturing perspective, achieving even sub-percent improvements at zero additional material cost is still valuable, especially when the system is already near optimal performance. More importantly, the value of the ANN framework in this work is not limited to achieving a marginal performance gain over the best parametric case. The ANN serves as a high-fidelity predictive surrogate model, as evidenced by the very small discrepancies between ANN predictions and full numerical simulations reported in Table 10. This demonstrates that the trained ANN can reliably predict melting performance for unseen geometric configurations. Consequently, designers can explore the design space and estimate performance in a fraction of a second, rather than performing time-consuming CFD simulations for each new configuration. This is a major practical advantage for parametric design, rapid prototyping, and future optimization studies. In addition, the ANN model was employed for: (1) Sensitivity analysis, revealing the relative importance of geometric parameters, (2) Exploring continuous design spaces beyond the 27 discrete simulated designs, and (30 Supporting multi-objective decision-making (via TOPSIS), where trade-offs between early-time and late-time melting performance are relevant. Regarding performance comparisons at different charging times, Table 10 shows that: At 2.5 h, both HMO (0.575) and BMO (0.563) outperform the best parametric design (Design 5: 0.536), indicating superior early-stage charging behavior. However, at 5 h, Design 5 (0.906) surpasses HMO (0.847) and BMO (0.873). Importantly, FMO outperforms Design 5 at both 2.5 h and 5 h, confirming that the ANN-based optimization identifies a design that is globally superior across the full charging period, rather than being optimal only at a single time point.

Fig. 9 provides a comprehensive comparison between the three optimized energy storage designs (HMO, FMO, and BMO), three finned-designs (Finned-design 15, Finned-design 50, and Finned-design 80), and the base-free reference system over the charging period. The evolution of key thermal parameters, including liquid fraction, energy storage, temperature rise, and the partitioning of sensible and latent heat, is presented to highlight the improvements achieved through geometric optimization. The variation of liquid fraction in Fig. 9a clearly illustrates the acceleration of melting in all three optimized designs relative to the base-free system. After 2.5 h of charging, the liquid fraction reaches 0.575, 0.551, and 0.572 for HMO, FMO, and BMO, respectively, compared to only 0.250 for the base-free system. These values correspond to improvements of 130%, 120%, and 129%, respectively. After 5 h, the enhancements remain substantial: the liquid fraction for HMO, FMO, and BMO reaches 0.847, 0.913, and 0.881, while the base-free case reaches just 0.368, representing improvements of 130%, 148%, and 139%, respectively. The sharp initial rise in the optimized curves reflects the **strong conductive heat transfer** from the bases to the PCM, which initiates melting quickly and uniformly near the heated wall. As time progresses, the slope of the liquid fraction curves decreases due to **the reduction in temperature gradients** and the **completion of melting in the upper zones**, leaving only the bottom PCM regions to melt, which is a slower process. In contrast, the base-free system exhibits a gentle slope throughout, as heat transfer relies mainly on natural convection, which develops gradually. In addition to the base-free configuration, Fig. 9a also compares the optimized designs (HMO, FMO, and BMO) with three representative finned configurations

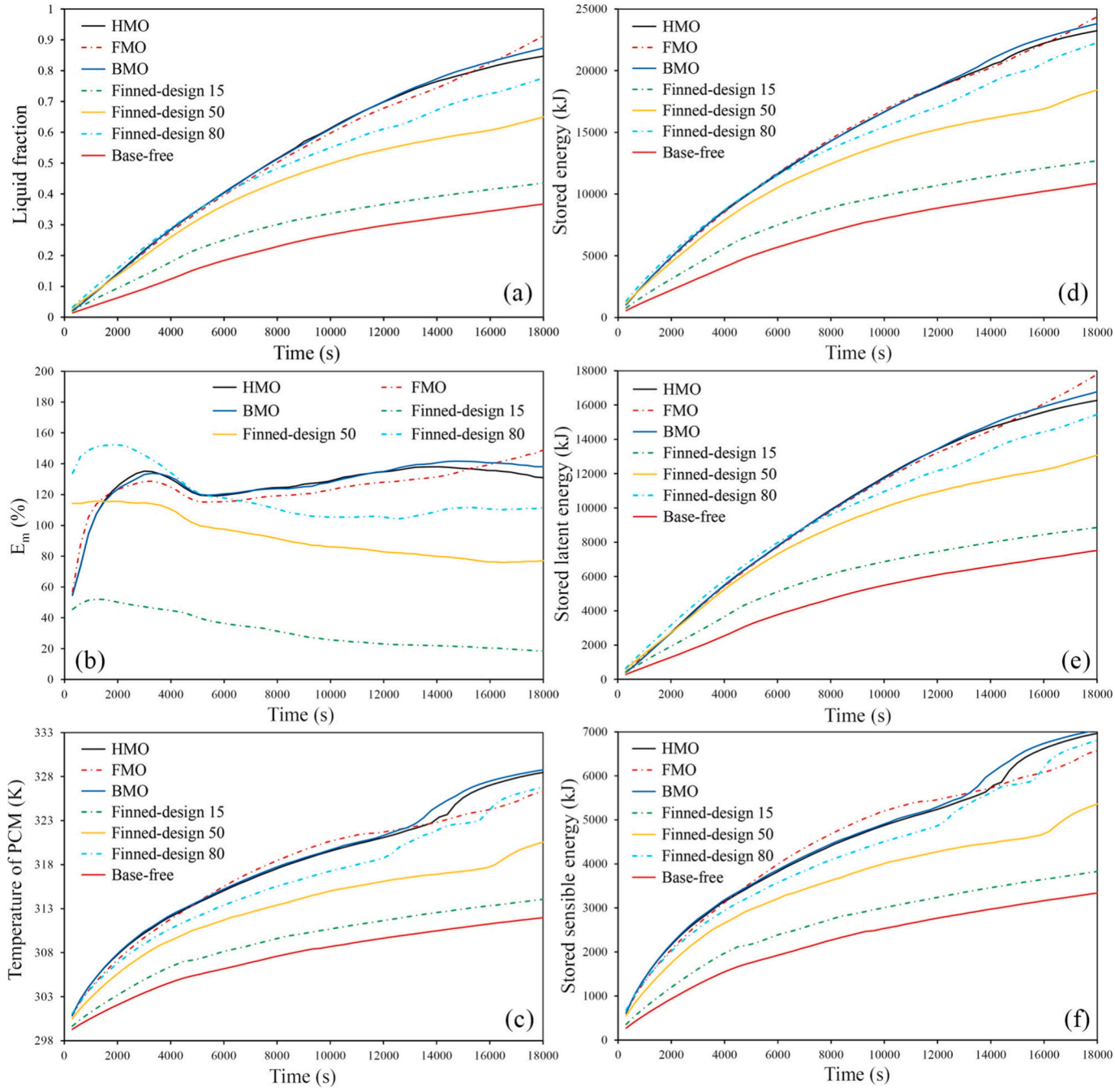


**Fig. 9.** Comparison of (a) liquid fraction, (b) melting enhancement ratio, (c) PCM temperature, (d) total stored energy, (e) stored latent energy, and (f) stored sensible energy between the three optimized designs (HMO, FMO, and BMO), three finned-designs (Finned-design 15, Finned-design 50, and Finned-design 80), and the base-free system.

(Finned-design 15, 50, and 80). As expected, adding fins enhances the melting rate compared to the base-free case by increasing the conductive heat transfer area. Among the finned configurations, Finned-design 80 shows the best performance due to its larger fin penetration length, followed by Finned-design 50 and Finned-design 15. Nevertheless, all finned designs remain clearly inferior to the optimized base-assisted configurations throughout the charging process. At 2.5 h, the liquid fraction of Finned-design 80 is about 0.517, whereas the optimized designs reach 0.575 (HMO), 0.551 (FMO), and 0.572 (BMO). This corresponds to performance improvements of approximately 11.2% (HMO vs. Finned-design 80), 6.6% (FMO vs. Finned-design 80), and 10.6% (BMO vs. Finned-design 80). The superiority of the optimized designs becomes even more pronounced at 5 h, where Finned-design 80 attains a liquid fraction of about 0.776, while HMO, FMO, and BMO reach 0.847, 0.913, and 0.881, respectively. These values indicate improvements of approximately 9.1% (HMO), 17.7% (FMO), and 13.5% (BMO) relative to the best finned configuration.

The $E_m$ curve in Fig. 9b quantifies the **percentage increase in melted volume** for each optimized design and finned design relative to the base-free case at the same time. All three optimized designs exhibit a rapid rise in $E_m$ during the initial stage, peaking at around **3000–4000 s and 14,000–18,000 s**, which corresponds to the **period of fastest melting acceleration** caused by the base structures.

➢ **HMO** reaches a **maximum $E_m$ of ~ 135%** at approximately **3000 s and** a **maximum $E_m$ of ~ 138%** at approximately **13,800 s**.

- ➢ **FMO** attains a slightly lower peak of **~129% at around 3300 s and a noticeable peak of ~ 149%** at around **18,000 s**.
- ➢ **BMO** exhibits peaks of ~134% at 3300 s and 142% at 1**4700 s**.

These peaks indicate the **maximum relative enhancement of melting** compared to the base-free system. At the very early stage, the optimized designs produce a rapid melting surge, causing $E_m$ to climb to its first maximum. As the melting front develops in the optimized cases, their instantaneous melting rates can temporarily slow down (latent-heat absorption becomes dominant and local temperature gradients are reduced), while the base-free case, although much weaker overall, may experience a relative acceleration as natural convection becomes established in its melt pool. This relative change produces the mid-time dip in $E_m$. Thereafter, the geometric advantages of the optimized configurations (improved conductive paths, advantageous tube placement, and greater sustained convective activation) reassert themselves. Hence, the optimized designs resume larger absolute melting rates compared with the base-free system. Because the base-free system never attains the same capacity to exploit conduction and convection, the ratio grows again, and $E_m$ increases in the late stage, i.e., the performance gap ultimately widens rather than collapses. For comparison, the best finned configuration (Finned-design 80) reaches a maximum $E_m$ of about 152.3% at ~1700 s. The reported peak value of 152.3% corresponds to the maximum enhancement in the melting process of Finned-design 80 relative to the base-free configuration. This high early-time enhancement reflects the strong initial conductive effect induced by the long fins, which accelerate the onset of melting near the heated regions. However, the enhancement ratio for Finned-design 80 decreases over time, indicating that the performance gap between the base-free and finned configuration progressively narrows as natural convection develops in the base-free system and the relative advantage of fins becomes less dominant. However, even the weakest finned configuration maintains a noticeable improvement over the base-free case. For instance, Finned-design 15 exhibits an enhancement of about 20% in melting at the end of the simulation, confirming that introducing fins consistently outperforms the base-free enclosure, albeit to a much smaller extent than the optimized base-assisted configurations.

The PCM temperature evolution in Fig. 9c follows the expected heating–melting transition pattern. All optimized designs show a rapid temperature rise during the first hour, reflecting strong heat conduction from the base plates into the PCM. Once melting begins, the temperature curve slope flattens as latent heat absorption dominates, stabilizing near the melting temperature range. The base-free system heats more slowly throughout due to the absence of conductive elements, leading to delayed melting and lower overall temperatures. The finned configurations display intermediate thermal behavior between the optimized and base-free designs. At 5 h, the average PCM temperatures reach 314.056 K for Finned-design 15, 320.554 K for Finned-design 50, and 326.810 K for Finned-design 80, confirming that increasing fin length enhances heat penetration into the PCM domain. Nevertheless, despite the elevated temperatures achieved by finned configurations, the optimized base-assisted designs still provide a more uniform and effective thermal response by promoting both conductive spreading and convective circulation within the molten PCM.

Based on Fig. 9d, the total stored energy profiles follow a similar trend to the liquid fraction curves, underscoring the enhanced charging efficiency of the optimized designs. At 2.5 h, HMO, FMO, and BMO store 15,516 kJ, 15707 kJ, and 15,500 kJ, respectively, compared to 7546 kJ for the base-free system, yielding improvements of approximately 106%, 108%, and 105%. At 5 h, these values increase to 23,236 kJ, 24359 kJ, and 23,810 kJ, while the base-free case reaches 10,852 kJ, corresponding to improvements of 114%, 124%, and 120%, respectively. Because FMO features shorter tilted bases, it accommodates a larger volume of PCM, enabling greater sensible heat storage. As a result, although HMO exhibits somewhat faster melting at the beginning, FMO eventually achieves higher total energy storage thanks to its increased PCM capacity and superior sensible heat absorption. The finned configurations again show improved performance compared to the base-free system, but they remain inferior to the optimized designs. At 2.5 h, the stored energies of Finned-design 15, 50, and 80 are 9401 kJ, 13294 kJ, and 14,600 kJ, respectively, whereas FMO stores 15,707 kJ. This corresponds to a performance improvement of approximately 67.1% over Finned-design 15, 18.2% over Finned-design 50, and 7.6% over Finned-design 80. At 5 h, the stored energy increases to 12,686 kJ (Finned-design 15), 18435 kJ (Finned-design 50), and 22,255 kJ (Finned-design 80), while FMO reaches 24,359 kJ. Accordingly, FMO exhibits an improvement of about 92.0% relative to Finned-design 15, 32.1% relative to Finned-design 50, and 9.5% relative to Finned-design 80.

Fig. 9e presents the evolution of stored latent energy, which directly reflects the extent and rate of PCM melting. As expected, all enhanced configurations (optimized bases and finned designs) significantly outperform the base-free system over the entire charging period, confirming that geometric modifications effectively intensify phase-change heat storage. Among all configurations, the optimized designs (HMO, FMO, and BMO) exhibit the highest latent energy storage at all times. This indicates that these designs not only accelerate the onset of melting but also sustain a higher melting rate throughout the process. The strong conductive pathways provided by the base plates rapidly transport heat into the PCM, while the favorable tube–base arrangement promotes more uniform melting fronts and stronger natural convection in the molten PCM. Consequently, the optimized designs convert a larger fraction of the supplied heat into latent heat, which is the most valuable storage mode in PCM-based TES systems. The finned designs exhibit intermediate performance. Increasing fin length from 15 to 80 mm systematically enhances latent energy storage, confirming that fins improve conductive heat penetration and accelerate the melting front. Finned-design 80 shows the best performance among the finned cases and approaches the optimized designs in the early and mid stages; however, it still remains noticeably below HMO, FMO, and BMO at long times. This indicates that while fins are effective in locally boosting conduction, they are less efficient than the optimized bases in establishing large-scale, system-wide conductive networks and sustained convective circulation within the PCM domain. The base-free configuration consistently stores the lowest latent energy throughout the process. In this case, melting is driven mainly by natural convection developing gradually near the heated wall, resulting in a delayed and spatially non-uniform phase-change front. The absence of any conductive enhancement severely limits the latent heat storage rate and capacity, highlighting the inherent weakness of the base-free design for rapid charging applications.

Fig. 9f depicts the evolution of stored sensible energy, which is associated with the temperature rise of the PCM before and during melting. The sensible energy curves reveal complementary but not identical trends to those of latent energy, since sensible storage depends more strongly on PCM temperature levels and total PCM mass, rather than purely on the melt fraction. The optimized designs again dominate the performance, with BMO attaining the highest sensible energy at long times, followed closely by HMO and FMO. The superior sensible heat storage of BMO is consistent with higher average PCM temperatures observed in Fig. 9c. The finned configurations show a clear monotonic improvement with fin length. Finned-design 80 stores considerably more sensible energy than Finned-design 50 and 15, which is in line with the higher PCM temperatures reached in Fig. 9c. Longer fins enhance heat diffusion deeper into the PCM, raising the bulk temperature and thereby increasing sensible heat storage. The base-free system exhibits the lowest sensible energy accumulation at all times, due to its weaker heating rate and lower average PCM temperature. The slow thermal penetration results in limited sensible energy storage, which, together with its poor latent heat performance, makes the base-free configuration the least effective design among all cases considered.

Fig. 10 presents the spatial evolution of the liquid fraction at five

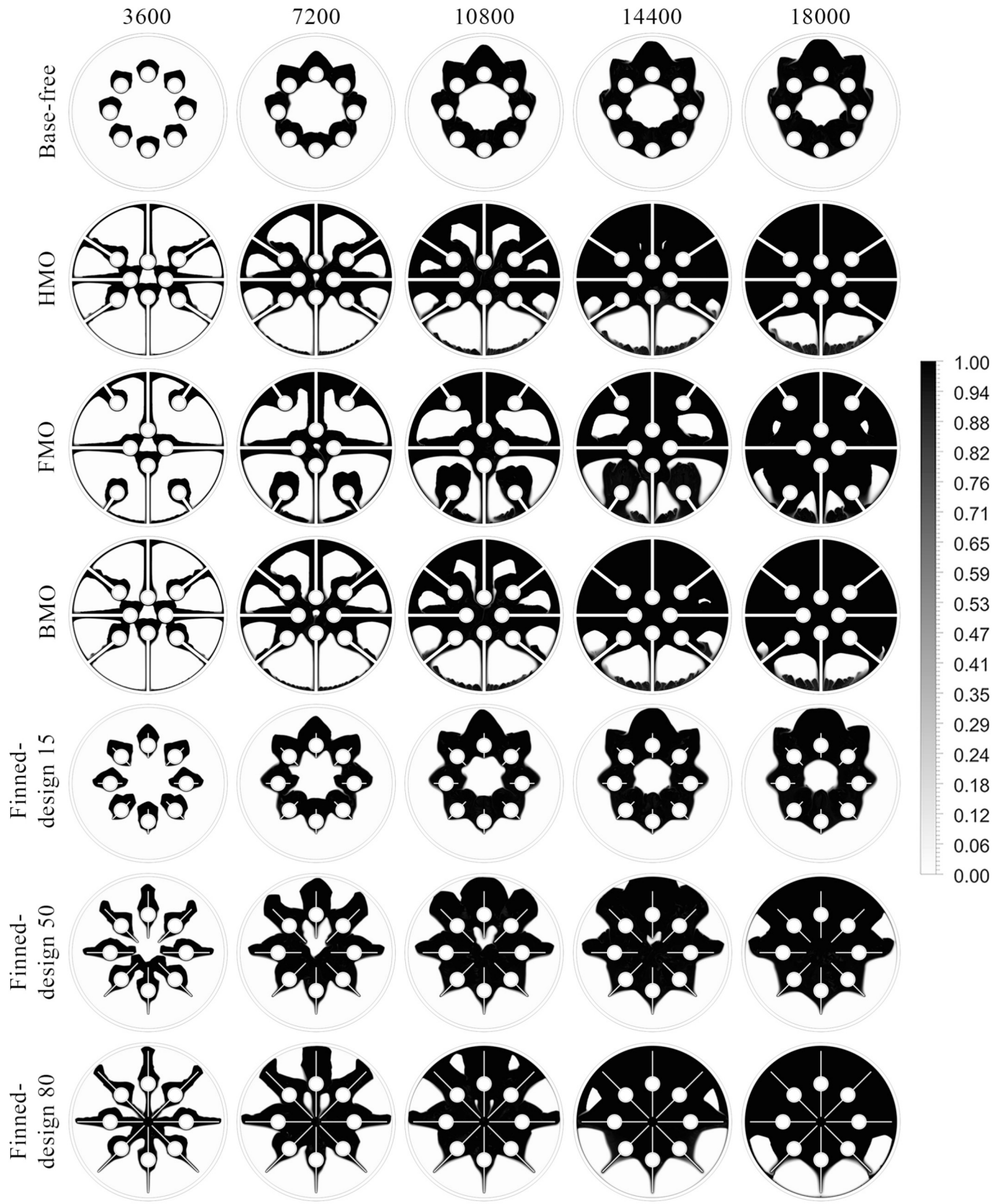


**Fig. 10.** Liquid fraction contours of PCM in seven energy storage systems: Base-free, HMO, FMO, BMO, Finned-design 15, Finned-design 50, and Finned-design 80.

time instants (3600, 7200, 10800, 14400, and 18,000 s) for the seven investigated configurations: base-free, three optimized designs (HMO, FMO, BMO), and three finned designs (15, 50, and 80 mm). In the base-free system, melting is first observed around the HTF tubes and at the upper part of the PCM box. As time progresses, the liquid PCM accumulates in the upper part due to buoyancy, while large solid PCM regions persist in the lower part of the box even at 18000 s. This behavior clearly reflects the dominance of natural convection: once a liquid layer forms near the heated surfaces, warmer, lighter liquid rises and stratifies at the top, leaving the bottom regions poorly supplied with heat. The absence of conductive pathways to the lower PCM results in strong thermal non-uniformity and delayed melting in the down parts of the box. The finned configurations enhance melting around the tubes by increasing the local heat transfer surface area. As fin length increases from 15 to 80 mm, the melted regions expand more rapidly and the liquid fraction contours become more extended radially. Finned-design 80 clearly performs better than finned-designs 15 and 50, showing larger melted regions at all times, which is consistent with the higher liquid fractions and stored energy observed in Fig. 9. However, despite the presence of fins, the lower parts of the PCM box remain partially

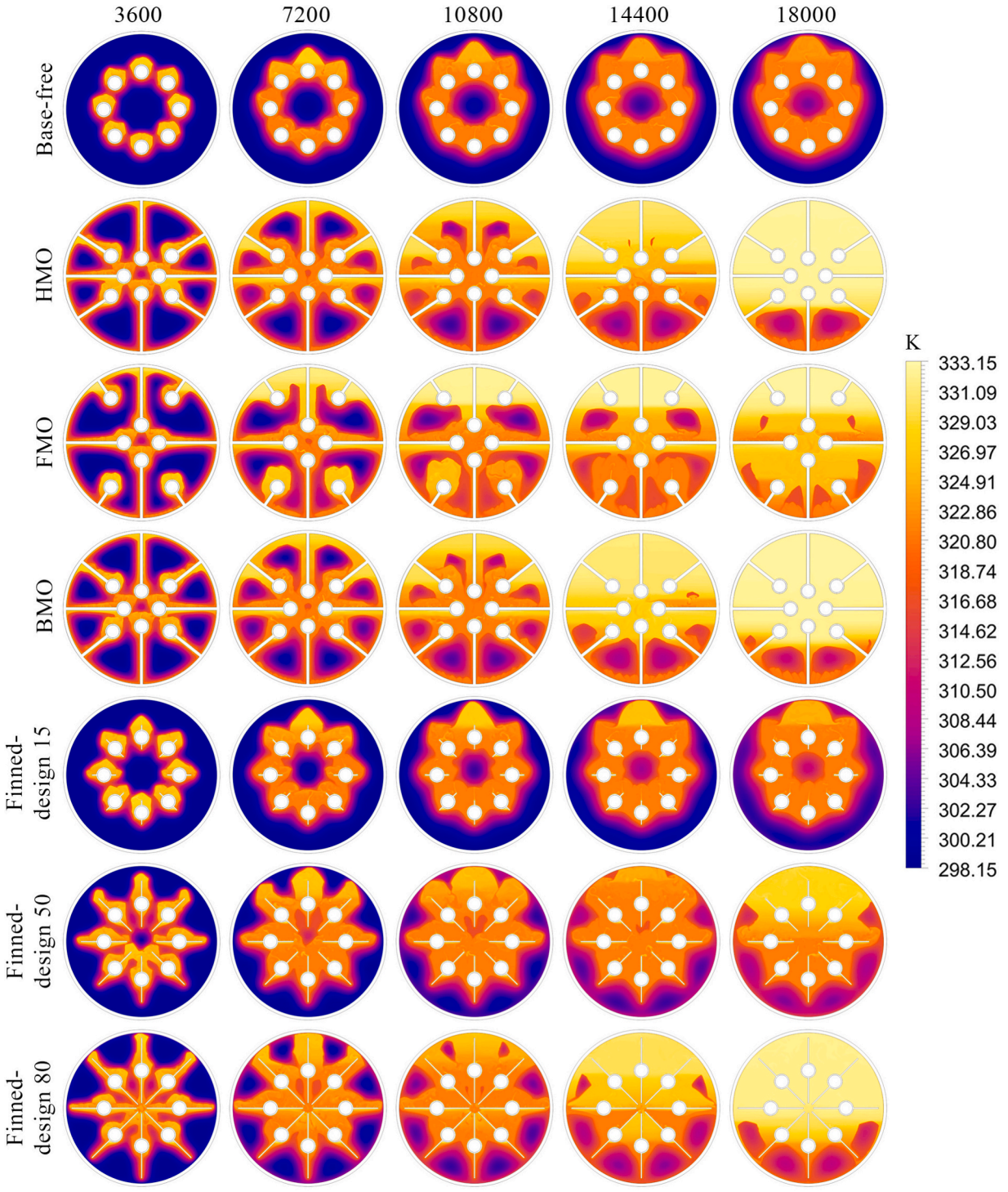


**Fig. 11.** Temperature distribution of PCM in seven energy storage systems: Base-free, HMO, FMO, BMO, Finned-design 15, Finned-design 50, and Finned-design 80.

unmolten even at the final charging time, particularly near the bottom of the shell. This highlights a fundamental limitation of the finned designs: although fins enhance conduction locally around the tubes, they are not connected to the outer shell. As a result, heat is not effectively delivered to the down parts of the PCM domain. Once melting begins near the tubes, buoyancy-driven flow carries liquid PCM upward, and the lower regions are progressively starved of both convective and conductive heat supply. Even in Finned-design 80, where fins are considerably longer, this geometric disconnection prevents efficient thermal communication with the shell, and unmolten PCM persists in the bottom regions. The three optimized configurations exhibit a fundamentally different melting pattern. In these designs, the HTF tubes are connected to the aluminum shell via bases, and the shell itself acts as an extended heat transfer surface. This creates a continuous conductive network from the heated tubes to the enclosure wall, enabling heat to be delivered directly to the lower regions of the PCM box. As a result, the melting fronts in HMO, FMO, and BMO are more uniform and more symmetric compared with both the base-free and finned cases. At early times, melting initiates not only around the tubes but also along the bases and shell, leading to a more distributed thermal penetration. At later times, the optimized designs show significantly reduced solid PCM remnants in the lower part of the enclosure, demonstrating that conduction through the bases and shell effectively compensates for the natural tendency of convection to preferentially melt the upper PCM regions. By altering the angle and length of these bases, the heat transfer paths are optimized for increased efficiency in the lower areas, which, as observed, exhibit less unmolten PCM. FMO could demonstrate a quicker melt in the bottom sections depending on the variation in the base structures. Despite the improvement over the base-free system, these designs still exhibit some unmolten areas at the bottom, hinting at the challenge of fully melting the PCM in the lower regions within a limited time frame.

Fig. 11 illustrates the transient temperature fields at 3600, 7200, 10800, 14400, and 18,000 s for the seven investigated configurations: base-free, HMO, FMO, BMO, finned-design 15, finned-design 50, and finned-design 80. These contours reveal how heat propagates within the PCM domain and clearly demonstrate the different thermal transport mechanisms activated by each structural design. In the base-free system, elevated temperatures remain confined to narrow regions surrounding the HTF tubes, while the majority of the PCM domain, particularly the lower and peripheral regions remain at relatively low temperatures throughout the charging process. Large cold zones (blue/purple regions) persist near the bottom of the box. This behavior reflects the weak conductive heat transfer pathways in the absence of bases or fins, causing the system to rely primarily on natural convection. Since convection develops gradually and preferentially transports heat upward, thermal penetration into the lower PCM regions is limited, resulting in pronounced temperature stratification and delayed melting. The finned configurations substantially increase the local temperature near the HTF tubes by extending the effective heat transfer area. As fin length increases from 15 to 80 mm, the high-temperature regions spread further into the PCM, and the thermal field becomes progressively more uniform around the tube array. Finned-design 80 exhibits the broadest warm region, confirming its superior thermal performance among the three finned cases. Nevertheless, even in finned-design 80, relatively cooler zones persist in the lower parts of the box, especially near the bottom of the shell. This indicates that although fins enhance radial heat spreading from the tubes, their inability to connect directly to the outer shell limits heat delivery to the down parts of the PCM domain. Consequently, the temperature field remains vertically non-uniform, and complete thermal homogenization is not achieved by fins alone. The optimized configurations display markedly different thermal patterns. In these cases, the HTF tubes are connected to the aluminum shell through bases, creating continuous conductive pathways. As a result, elevated temperatures rapidly extend from the tubes to the shell and then spread along the enclosure wall. This leads to a much more uniform temperature distribution across the PCM domain, particularly in the lower regions that are poorly heated in the base-free and finned designs. At early times (3600–7200 s), HMO, FMO, and BMO already exhibit extensive warm zones distributed along the bases and shell, indicating strong conductive heat transfer. At later times (14400–18,000 s), large portions of the PCM domain approach near-uniform high temperatures, confirming that the optimized geometries significantly enhance heat propagation. In HMO and BMO, the upper regions of the storage exhibit significantly higher temperatures compared to the lower parts, whereas FMO demonstrates a more uniform temperature distribution, though its overall temperatures remain lower. The corresponding temperature profiles also support this observation.

### 6.4. Comparative assessment of the proposed design with state-of-the-art TSDs

Table 11 presents a comparative evaluation of the proposed Full-Melting Optimal (FMO) design with several latent heat thermal energy storage systems reported in the literature. The comparison is performed using the temperature difference between the HTF and the PCM liquidus temperature ($T_{HTF}$-$T_{PCM\text{-}liquidus}$) and the time required to reach a liquid fraction of $\varphi \geq 0.9$. Since faster melting indicates more effective heat transfer and faster charging of the storage system, shorter melting times correspond to better thermal performance. The results show that the FMO design in the present study reaches $\varphi \geq 0.9$ in 17,730 s using lauric acid with a temperature difference of 11.8 K. This performance is competitive with many previously reported TES configurations. For example, the shell-and-tube TES system reported by Li et al. [62] required 13,592 s to reach a similar melting fraction with a larger temperature difference of 14 K. Although the melting time is shorter, it should be noted that the driving temperature difference in that study is approximately 18.6% higher than that used in the present work, which naturally accelerates the melting process. In contrast, other shell-and-tube systems demonstrate significantly longer melting durations. For instance, the system studied by Ghalambaz et al. [65] required 22,709 s, meaning that the FMO design achieves the same melting fraction about 22% faster. It is emphasized that direct quantitative comparison across different studies is inherently influenced by variations in system scale, PCM volume, boundary conditions, and HTF operating parameters.

**Table 11**
Comparison of the thermal performance of the proposed Full-Melting Optimal (FMO) design with representative latent heat thermal energy storage (TES/LHS) systems reported in the literature.

| Study | Storage design | PCM | $T_{HTF}$-$T_{PCM\text{-}liquidus}$ (K) | Time for $\varphi \geq 0.9$ (s) |
|---|---|---|---|---|
| Present study | FMO | Lauric acid | 11.8 | 17,730 |
| Li et al. [59] | Shell-and-tube TES | RT50 | 14 | 13,592 |
| Ghalambaz et al. [65] | Shell-and-tube TES | Coconut oil | 25.85 | 22,709 |
| Xu et al. [66] | TTHE | RT60 | 10 | 2550 |
| *Al*-Abidi et al. [67] | TTHE | RT82 | 5 | 2220 |
| Yan et al. [68] | Compact-TES with ribs | RT42 | 23 | 9003 |
| Zheng et al. [69] | Compact-LHS with fins | RT42 | 11.1 | 10,880 |
| Gurel et al. [70] | P-LHS | n-octadecane | 33.65 | 2100 |
| Deng et al. [71] | Multi-section LHS | RT50 | 14 | 10,637 |
| Cui et al. [72] | TTHE with radial fins | RT50 | 24 | 1166 |
| Vogel et al. [73] | Finned-LHS | NaNo3 | 10 | 5400 |
| Vaferi et al. [5] | TES tank | RT50 | 19 | 14,700 |
| Esmaeili et al. [74] | TTHE with tree-shaped fins | RT82 | 5 | 2416 |
| Ran et al. [37] | TTHE with fins | Lauric acid | 21.8 | 1619 |

Nevertheless, the consistent improvement observed in melting rate indicates that the proposed FMO design not only outperforms conventional baseline geometries but also competes favorably with more complex enhancement strategies reported in the literature. These results clearly demonstrate the necessity and effectiveness of the optimization framework adopted in this study and validate the superiority of the proposed base-integrated design for accelerating PCM charging under realistic driving temperature differences.

## 7. Conclusions

This study introduces and systematically evaluates a novel, base-integrated energy storage system designed to enhance thermal efficiency. Unlike conventional shell-and-tube configurations, the proposed design integrates HTF tubes directly into the PCM box and supports them with adjustable straight and tilted bases. Through comprehensive numerical simulations covering 27 distinct geometric configurations, it was demonstrated that base geometry plays a decisive role in accelerating PCM melting. An ANN-based predictive model was developed to map the relationship between geometric parameters and melting behavior efficiently. By coupling this model with a GA, both single-objective and multi-objective optimizations were performed to identify designs that maximize liquid fraction. The Pareto front analysis provided a range of optimal solutions that balance early-stage and long-duration performance. Besides, three additional engineered Finned-designs were introduced to be compared with the optimal designs. Based on the findings:

- The results of both the parity plots and cross-validation jointly validate the robustness of the proposed ANN model. The combination of high $R^2$ values, low RMSE, and consistent accuracy across different folds ensures that the model avoids overfitting while maintaining excellent generalization.
- Adjusting the straight and tilted base lengths, as well as their inclination angles, significantly improved heat transfer, resulting in more uniform melting and larger liquid fractions. Among the investigated parameters, the length of the straight bases was the most significant parameter, consistently influencing the liquid fraction.
- By the end of the 5-h charging period, the highest liquid fraction among the 27 parametric configurations was achieved by Design 5, reaching a value of 0.906, whereas the base-free design attained a liquid fraction of only 0.368. This indicates that Design 5 enhances the melting performance by approximately 146% compared to the base-free configuration. A similar trend is observed in terms of total stored energy. After 5 h, Design 5 stores 23,944 kJ of thermal energy, while the base-free system stores only 10,852 kJ. This corresponds to an improvement of approximately 120.6% in total absorbed energy for Design 5 relative to the base-free design.
- In the first step of the GA process, **single-objective optimization** was performed. Two distinct objectives were set: (1) Maximization of the liquid fraction at **2.5 h**, and (2) Maximization of the liquid fraction at **5 h**. The GA algorithm yielded two optimal geometric configurations: **Half-Melting Optimal (HMO) for the first objective and Full-Melting Optimal (FMO) for the second**.
- The TOPSIS-selected design, named Balanced-Melting Optimal (BMO), had a closeness coefficient of 0.667; falling between the values of HMO and FMO, as expected for a balanced design.
- After 5 h of charging, the liquid fraction reaches 0.847, 0.913, and 0.881 for HMO, FMO, and BMO, respectively, compared to only 0.368 for the base-free system. These values correspond to improvements of 130%, 148%, and 139%, respectively.
- At 5 h, HMO, FMO, and BMO stored 23,236 kJ, 24359 kJ, and 23,810 kJ, respectively, compared to 10,852 kJ for the base-free system, yielding improvements of approximately 114%, 124%, and 120%.
- Among the optimized configurations, FMO was proposed as the best overall optimal design, since it achieved the highest performance in terms of both liquid fraction and total stored energy. When compared directly with Design 5, the FMO configuration still provided measurable improvements, with approximately 0.77% betterment in liquid fraction and about 1.73% in stored energy.

## CRediT authorship contribution statement

**Jun-Bo Mao:** Supervision, Investigation. **Ali Basem:** Investigation, Data curation. **Hyder H. Abed Balla:** Investigation, Formal analysis. **Yong-hui Li:** Writing – review & editing, Writing – original draft. **Omar J. Alkhatib:** Formal analysis, Data curation. **M.A. Ahmed:** Resources, Funding acquisition. **Sherzod Abdullaev:** Writing – original draft, Investigation. **Hind Albalawi:** Project administration, Funding acquisition. **Zuhair Jastaneyah:** Writing – review & editing, Resources, Investigation. **Ibrahim Mahariq:** Supervision, Methodology, Conceptualization.

## Declaration of competing interest

The authors declare that they have no known competing financial interests or personal relationships that could have appeared to influence the work reported in this paper.

## Acknowledgement

The project was supported by the Key Project of Philosophy and Social Sciences in Yunnan Province: “Research on Rule Coordination and Governance Innovation in China-Myanmar Cross-Border Data Flow (ZD202525)”. The authors extend the appreciation to the Deanship of Postgraduate Studies and Scientific Research at Majmaah University for funding this research work through the project number (R-2026-30). Princess Nourah bint Abdulrahman University Researchers Supporting Project number (PNURSP2026R29), Princess Nourah bint Abdulrahman University, Riyadh, Saudi Arabia.

## Data availability

The authors do not have permission to share data.

## References

[1] Y.-C. Tsao, I.G.A. Banyupramesta, J.-C. Lu, Optimal operation and capacity sizing for a sustainable shared energy storage system with solar power and hydropower generator, J. Energy Storage 110 (2025) 115173, https://doi.org/10.1016/j.est.2024.115173.
[2] N. Mohd Aripin, S. Hussain, L. Khai Loon, F. Mahmud, N.S.N. Alimin, The integration of energy storage system in solar power generation: a bibliometric perspective of renewable energy, Int. J. Energy Sect. Manag. (2025), https://doi.org/10.1108/IJESM-10-2024-0050.
[3] M. Zheng, Z. Wu, T. Liu, S. Yan, X. Li, G. Jiang, et al., Optimization of microcrack control and performance in Deepwater well cementing with microencapsulated phase change materials, Geoenergy Sci. Eng. 257 (2026) 214220, https://doi.org/10.1016/j.geoen.2025.214220.
[4] Y. Chen, A. Sha, Q. Lu, W. Jiang, Y. Cao, K. Hu, et al., Solar-to-heat conversion control of pavement through thermochromic coating: integration of thermal management and visual temperature indication, Energy 333 (2025) 137383, https://doi.org/10.1016/j.energy.2025.137383.
[5] K. Vaferi, S. Nekahi, S. Nekahi, H. Ghaebi, Charging/discharging performance examination in a finned-tube heat storage tank: based on artificial neural network, pareto optimization, and numerical simulation, Case Stud. Therm. Eng. (2025) 106388, https://doi.org/10.1016/j.csite.2025.106388.
[6] B. Bai, T. Xu, Q. Nie, P. Li, Temperature-driven migration of heavy metal Pb2+ along with moisture movement in unsaturated soils, Int. J. Heat Mass Transf. 153 (2020) 119573, https://doi.org/10.1016/j.ijheatmasstransfer.2020.119573.
[7] S.A. Abdollahi, A. Basem, A. Alizadeh, D.J. Jasim, M. Ahmed, A.J. Sultan, et al., Combining artificial intelligence and computational fluid dynamics for optimal design of laterally perforated finned heat sinks, Results Eng. 21 (2024) 102002, https://doi.org/10.1016/j.rineng.2024.102002.
[8] J. Liu, C. Ma, M. Li, J. He, G. Totis, C. Hua, et al., A real-time spatiotemporal error compensation framework for face gear grinding, Eng. Appl. Artif. Intell. 162 (2025) 112429, https://doi.org/10.1016/j.engappai.2025.112429.

[9] Z. Zhan, L. Lin, J. Zhang, Z. Li, Q. Zhang, Q. Wang, Effect of in situ polymerization on the thermal stability and enthalpy properties of wood-based composites based on graphene oxide–modified phase change microcapsule, Polym. Compos. 46 (2025) 15342–15356, https://doi.org/10.1002/pc.30133.
[10] M. Cui, D. Han, H. Liu, K.-C. Li, M. Tang, C.-C. Chang, et al., Secure data sharing for consortium blockchain-enabled vehicular social networks, IEEE Trans. Veh. Technol. 73 (2024) 19682–19695, https://doi.org/10.1109/TVT.2024.3448207.
[11] S. Nekahi, F.S. Moghanlou, M. Vajdi, K. Vaferi, S. Nekahi, T. Gholizadeh, Development and performance evaluation of a honeycomb-structured shell-and-tube thermal storage system integrating a series of openings on the hexagonal cells for enhanced energy absorption/release, Int Commun Heat Mass Transf 173 (2026) 110897, https://doi.org/10.1016/j.icheatmasstransfer.2026.110897.
[12] X. Hu, B. Quan, Z. Shi, X. Zhao, G. Lu, Y. Ding, et al., Bioinspired hierarchical radiative-phase change hybrid cooling composite with record-breaking cooling power, Adv. Mater. 38 (2026), https://doi.org/10.1002/adma.202510988.
[13] H. Chu, W. Chen, L. Deng, Refined segmentation of high-resolution bridge crack images via probability map-guided point rendering technique, Comput Civ Infrastruct Eng 40 (2025) 4946–4969, https://doi.org/10.1111/mice.70088.
[14] M. Shehram, M.N. Hamidi, A.A. Abdul Wahab, M.K. Mat Desa, Experimental development of hybrid nitride-based PCM with sand stones for enhanced thermal energy storage, Mater. Sci. Semicond. Process. 198 (2025) 109789, https://doi.org/10.1016/j.mssp.2025.109789.
[15] K. Vaferi, M. Vajdi, S. Nekahi, A. Heydari, F. Sadegh Moghanlou, H. Nami, et al., Thermo-hydraulic performance optimization of a disk-shaped microchannel heat sink applying computational fluid dynamics, artificial neural network, and response surface methodology, Heliyon 9 (2023) e21031, https://doi.org/10.1016/j.heliyon.2023.e21031.
[16] G. Wang, J. Liu, Design and performance evaluation of a novel photovoltaic and concentrated solar thermal system using parabolic trough-shaped spectrum filter, Energy Sources, Part A Recover Util Environ Eff 47 (2025) 6918–6933, https://doi.org/10.1080/15567036.2025.2476119.
[17] G. Wang, S. Zhang, T. Zou, Design and comparison study of a novel linear Fresnel reflector solar ORC-driven hydrogen production system using different working fluids, Case Stud. Therm. Eng. 71 (2025) 106187, https://doi.org/10.1016/j.csite.2025.106187.
[18] C. Tu, C. Zhu, M. Sun, X. Hu, L. Zhou, X. Zhao, et al., Engineered thermal conduction pathways in high-performance flexible PEG phase-change composites enabling efficient thermal storage and thermoelectric conversion, Chem. Eng. J. 528 (2026) 172574, https://doi.org/10.1016/j.cej.2026.172574.
[19] K.A. Hammoodi, H.A. Hasan, M.H. Abed, A. Basem, A.M. Al-Tajer, Control of heat transfer in circular channels using oblique triangular ribs, Results Eng. 15 (2022) 100471, https://doi.org/10.1016/j.rineng.2022.100471.
[20] G. Wang, D. Li, T. Zou, Y. Duan, Design and performance evaluation of an innovative solar concentration polygeneration system, Renew. Energy 251 (2025) 123441, https://doi.org/10.1016/j.renene.2025.123441.
[21] G. Wang, J. Hao, B. Wang, W. Han, Comparative study on thermal and mechanical performances of liquid lead thermocline heat storage tank with different solid filling material layouts, Case Stud. Therm. Eng. 73 (2025) 106754, https://doi.org/10.1016/j.csite.2025.106754.
[22] B. Bai, F. Bai, Q. Nie, X. Jia, A high-strength red mud–fly ash geopolymer and the implications of curing temperature, Powder Technol. 416 (2023) 118242, https://doi.org/10.1016/j.powtec.2023.118242.
[23] C. Wang, S. Yao, X. Chen, X. Yan, X. Zhan, Thermal performance analysis of arc-shaped fins of horizontal latent heat thermal energy storage system, Int. J. Heat Fluid Flow 112 (2025) 109748, https://doi.org/10.1016/j.ijheatfluidflow.2025.109748.
[24] Z. He, H. Ma, S. Lu, Design and experimental investigation of topology-optimized fin structures for enhanced heat transfer in latent heat thermal energy storage units, J. Energy Storage 80 (2024) 110272, https://doi.org/10.1016/j.est.2023.110272.
[25] S. Tang, Y. Song, P. Liu, X. Wu, Y. Xu, J. Zhou, et al., Design and optimization of a vertical shell-and-tube latent heat thermal energy storage system via discontinuous fins, Renew. Energy 243 (2025) 122568, https://doi.org/10.1016/j.renene.2025.122568.
[26] T. Abdulrazzaq, H. Togun, J.M. Mahdi, H.I. Mohammed, F.L. Rashid, A.F. Khalaf, et al., Evaluation of multi-branch fin inserts for improved thermal response in latent heat storage systems: a numerical approach, Case Stud. Therm. Eng. 73 (2025) 106464, https://doi.org/10.1016/j.csite.2025.106464.
[27] S.A. Marzouk, F.A. Almehmadi, A. Aljabr, M.O. Hamdan, M.A. Sharaf, Enhancing melting of phase change material in double tube latent heat storage system by pin fins, ASME J. Heat Mass Transf. 147 (2025), https://doi.org/10.1115/1.4068160.
[28] K. Vaferi, A. Farajollahi, T. Gholizadeh, M. Rostami, Enhancing charging and discharging performance in a novel latent heat storage via design optimization and artificial neural network modeling, J. Energy Storage 114 (2025) 115757, https://doi.org/10.1016/j.est.2025.115757.
[29] Z. Chen, B. Li, B. Wang, Robust stability Design for Inverters Using Phase lag in proportional-resonant controllers, IEEE Trans. Ind. Electron. 72 (2025) 2655–2668, https://doi.org/10.1109/TIE.2024.3436639.
[30] F. Ren, P.-Z. Zhuang, X. Chen, H.-S. Yu, H. Yang, Physics-informed extreme learning machine (PIELM) for Stefan problems, Comput. Methods Appl. Mech. Eng. 441 (2025) 118015, https://doi.org/10.1016/j.cma.2025.118015.
[31] B. Bai, F. Bai, X. Li, Q. Nie, X. Jia, H. Wu, The remediation efficiency of heavy metal pollutants in water by industrial red mud particle waste, Environ. Technol. Innov. 28 (2022) 102944, https://doi.org/10.1016/j.eti.2022.102944.
[32] S. Nekahi, F. Sadegh Moghanlou, K. Vaferi, H. Ghaebi, M. Vajdi, H. Nami, Optimizing finned-microchannel heat sink design for enhanced overall performance by three different approaches: numerical simulation, artificial neural network, and multi-objective optimization, Appl. Therm. Eng. 245 (2024) 122835, https://doi.org/10.1016/j.applthermaleng.2024.122835.
[33] Z. Li, L. Wu, M. Shaban, A.M. Abed, Z.A. Bu sinnah, A. Almadhor, et al., Advanced latent thermal energy storage design featuring three dividers: optimizing multi-enclosure system with ANN-driven models and hybrid phase change material integration, J. Energy Storage 122 (2025) 116603, https://doi.org/10.1016/j.est.2025.116603.
[34] C. Yan, P. Kumar Singh, O. Hamlaoui, Hajji M karim, Y. Elmasry, Redhee A huseen, et al., Heat release efficiency betterment inside a novel-designed latent heat exchanger featuring arc-shaped fins and a rotational mechanism via numerical model and artificial neural network, Case Stud. Therm. Eng. 61 (2024) 105093, https://doi.org/10.1016/j.csite.2024.105093.
[35] A. Almadhor, A. Basem, P.K. Singh, N.A. Othman, S. Samad, F.M. Alhomayani, et al., Optimizing novel thermal energy storage systems: enhancing melting efficiency with tubes, stands, and advanced machine learning techniques, J. Energy Storage 124 (2025) 116908, https://doi.org/10.1016/j.est.2025.116908.
[36] F. Agyenim, P. Eames, M. Smyth, Heat transfer enhancement in medium temperature thermal energy storage system using a multitube heat transfer array, Renew. Energy 35 (2010) 198–207, https://doi.org/10.1016/j.renene.2009.03.010.
[37] L. Ran, G. Yan, V. Goyal, S. Abdullaev, F.M. Alhomayani, L.T. Le, et al., Advancing solar thermal utilization by optimization of phase change material thermal storage systems: a hybrid approach of Artificial Neural Network (ANN)/Genetic Algorithm (GA), Case Stud. Therm. Eng. 64 (2024) 105513, https://doi.org/10.1016/j.csite.2024.105513.
[38] B. Kamkari, H. Shokouhmand, F. Bruno, Experimental investigation of the effect of inclination angle on convection-driven melting of phase change material in a rectangular enclosure, Int. J. Heat Mass Transf. 72 (2014) 186–200, https://doi.org/10.1016/j.ijheatmasstransfer.2014.01.014.
[39] B. Huang, L.-L. Tian, Q.-H. Yu, X. Liu, Z.-G. Shen, Numerical analysis of melting process in a rectangular enclosure with different fin locations, Energies 14 (2021) 4091, https://doi.org/10.3390/en14144091.
[40] A.A. Tseng, Y.-T. Chen, K.-J. Ma, Fabrication of high-aspect-ratio microstructures using excimer laser, Opt. Lasers Eng. 41 (2004) 827–847, https://doi.org/10.1016/S0143-8166(03)00062-9.
[41] A.W. Kandeal, M. Ismail, A. Basem, M.M. Elsayad, W.H. Alawee, H.S. Majdi, et al., An overview of the improvement of natural convection heat transfer via surface thermal radiation for different geometries, Results Eng. 23 (2024) 102514, https://doi.org/10.1016/j.rineng.2024.102514.
[42] K. Vaferi, M. Vajdi, A. Shadian, H. Ahadnejad, F.S. Moghanlou, H. Nami, et al., Modeling and optimization of hydraulic and thermal performance of a tesla valve using a numerical method and artificial neural network, Entropy 25 (2023) 967, https://doi.org/10.3390/e25070967.
[43] C. Prieto, E. Borri, M.C. Pavon-Moreno, G. Zsembinszki, L.F. Cabeza, A technical and economic comparison between concrete and latent thermal energy storage for concentrated solar power applications, Appl. Therm. Eng. 275 (2025) 126823, https://doi.org/10.1016/j.applthermaleng.2025.126823.
[44] H. Chu, J. Gai, W. Chen, J. Ma, CBRFormer: rendering technology-based transformer for refinement segmentation of bridge crack images, Adv. Eng. Inform. 69 (2026) 103868, https://doi.org/10.1016/j.aei.2025.103868.
[45] W. Zhao, J. Chen, H. Jiang, M. Li, R. Liu, Y. Gao, et al., TiN supported 3D directional tubular skeleton encapsulating phase change materials for efficient solar-thermal energy conversion and storage, Sol. Energy 302 (2025) 114071, https://doi.org/10.1016/j.solener.2025.114071.
[46] J. Fan, X. Zhang, N. He, F. Song, X. Wang, Investigation on novel deep eutectic solvents with high carbon dioxide adsorption performance, J. Environ. Chem. Eng. 13 (2025) 117870, https://doi.org/10.1016/j.jece.2025.117870.
[47] B. Bai, J. Chen, F. Bai, Q. Nie, X. Jia, Corrosion effect of acid/alkali on cementitious red mud-fly ash materials containing heavy metal residues, Environ. Technol. Innov. 33 (2024) 103485, https://doi.org/10.1016/j.eti.2023.103485.
[48] H. Su, E. Zio, Z.-J. Zhang, C.-Z. Xiong, Q.-S. Dai, Q.-W. Wu, et al., Development of an integrated dynamic model for supply security and resilience analysis of natural gas pipeline network systems, Pet. Sci. 19 (2022) 761–773, https://doi.org/10.1016/j.petsci.2021.10.002.
[49] M. Benaissa, H.S. Sultan Aljibori, S.P. Nemat, S. Saadaoui, A.E. Tiji, J.M. Mahdi, et al., Optimizing the shell-and-multitube latent heat thermal storage: influence of tube layout and fin design on consecutive/simultaneous operation modes, Int Commun Heat Mass Transf 167 (2025) 109301, https://doi.org/10.1016/j.icheatmasstransfer.2025.109301.
[50] A. Farajollahi, K. Vaferi, M. Baharvand, Analyzing tube arrangements of a finned-tube heat exchanger to optimize overall efficiency using artificial neural network and response surface methodology, Case Stud. Therm. Eng. 63 (2024) 105302, https://doi.org/10.1016/j.csite.2024.105302.
[51] S. Luo, K. Zhang, L. Wang, Q. Zhang, Z. Hu, G. Shi, et al., Numerical study of heat transfer characteristics of rectangular latent heat thermal energy storage unit, Therm. Sci. Eng. Prog. (2025) 104143, https://doi.org/10.1016/j.tsep.2025.104143.
[52] A. Shafee, A. Basem, H.A.Z. AL-bonsrulah, S. Althobaiti, S.M.Y. Mohamed, Thermal management of NEPCM during freezing considering conduction mechanism, J. Therm. Anal. Calorim. 149 (2024) 14355–14371, https://doi.org/10.1007/s10973-024-13717-0.
[53] N. Kousha, M. Rahimi, R. Pakrouh, R. Bahrampoury, Experimental investigation of phase change in a multitube heat exchanger, J. Energy Storage 23 (2019) 292–304, https://doi.org/10.1016/j.est.2019.03.024.

[54] M. Ghalambaz, A.H. Eisapour, H.I. Mohammed, M.S. Islam, O. Younis, P.T. Sardari, et al., Impact of tube bundle placement on the thermal charging of a latent heat storage unit, Energies 14 (2021) 1289, https://doi.org/10.3390/en14051289.
[55] Z. Gao, Z. Wei, W. Liu, L. Zhang, S. Wen, G. Guo, Global prescribed performance control for 2-D plane vehicular platoons with small overshoot: a fixed-time composite sliding mode control approach, IEEE Trans. Intell. Transp. Syst. 26 (2025) 18789–18804, https://doi.org/10.1109/TITS.2025.3595130.
[56] J. Shafi, O. Younis, S. Tiari, M. Ghalambaz, Artificial intelligence – numerical study of melting and solidification heat transfer in a bundle of petal tubes embedded in metal foam, Appl. Therm. Eng. 279 (2025) 127960, https://doi.org/10.1016/j.applthermaleng.2025.127960.
[57] S.M. Arab, S. Nekahi, F. Sadegh Moghanlou, M. Vajdi, Z. Ahmadi, M. Shahedi Asl, A novel TiB2–SiC composite doped with diamond nanoparticles: densification, microstructure, and thermal properties, JOM (2024), https://doi.org/10.1007/s11837-024-07017-z.
[58] Y. Zhang, H. Yu, Y. Hou, N. Zhu, Multi-objective optimization research based on NSGA-II and experimental study of triplex-tube phase change thermal energy storage system, Energies 18 (2025) 2129, https://doi.org/10.3390/en18082129.
[59] Y. Li, A. Basem, S. Alhumaid, R. Ghandour, Z. Bayhan, X. Li, et al., Performance-cost co-optimization of shell-and-tube thermal energy storage units with enhanced sub-fin geometry via a hybrid numerical–AI approach, J. Energy Storage 144 (2026) 119655, https://doi.org/10.1016/j.est.2025.119655.
[60] Z. Xu, L. Qi, H. Du, J. Yang, Z. Chen, AlignFusionNet: efficient cross-modal alignment and fusion for 3D semantic occupancy prediction, IEEE Access 13 (2025) 125003–125015, https://doi.org/10.1109/ACCESS.2025.3589858.
[61] T. Javanbakht, Optimization of beverage formulation with technique for order of preference by similarity to ideal solution, Beverages 11 (2025) 38, https://doi.org/10.3390/beverages11020038.
[62] R. Li, J. Ma, X. Zhang, X. Shi, W. Sun, X. Lu, Modeling and analysis of relative fatigue life under 3D mixed lubrication in marine helical gears, Tribol. Int. 211 (2025) 110834, https://doi.org/10.1016/j.triboint.2025.110834.
[63] H. Alhammadi, M. Alghailani, N. Alkhzaimi, D. Alsuwaidi, A. Mayyas, Multi-criteria decision-making methods for selecting the best energy storage systems in arid regions, Energy Rep. 13 (2025) 3575–3592, https://doi.org/10.1016/j.egyr.2025.03.026.
[64] K.P. Patel, T.M. Patel, Analysis, evaluation and selection of nanoparticles added in paraffin using the MADM-TOPSIS approach, Interactions 246 (2025) 59, https://doi.org/10.1007/s10751-025-02281-0.
[65] M. Ghalambaz, S.A.M. Mehryan, A. Hajjar, M.Y. Al Shdaifat, O. Younis, P. Talebizadehsardari, et al., Thermal charging optimization of a wavy-shaped nano-enhanced thermal storage unit, Molecules 26 (2021) 1496, https://doi.org/10.3390/molecules26051496.
[66] H. Xu, N. Wang, C. Zhang, Z. Qu, M. Cao, Optimization on the melting performance of triplex-layer PCMs in a horizontal finned shell and tube thermal energy storage unit, Appl. Therm. Eng. 176 (2020) 115409, https://doi.org/10.1016/j.applthermaleng.2020.115409.
[67] A.A. Al-Abidi, S. Mat, K. Sopian, M.Y. Sulaiman, A.T. Mohammad, Internal and external fin heat transfer enhancement technique for latent heat thermal energy storage in triplex tube heat exchangers, Appl. Therm. Eng. 53 (2013) 147–156, https://doi.org/10.1016/j.applthermaleng.2013.01.011.
[68] G. Yan, J. Li, R.N. Dara, M. Shaban, R. Ghandour, F.M. Alhomayani, et al., Solar-powered compact thermal energy storage system with rapid response time and rib-enhanced plate via techniques of CFD, ANN, and GA, J. Energy Storage 105 (2025) 114807, https://doi.org/10.1016/j.est.2024.114807.
[69] Z. Zheng, G. Yan, A.M. Abed, M.A. Alghassab, B. Abdullaeva, F.M. Alhomayani, et al., Optimizing and investigating the charging time of phase change materials in a compact-latent heat storage using pareto front analysis, artificial neural networks, and numerical simulations, J. Energy Storage 102 (2024) 113966, https://doi.org/10.1016/j.est.2024.113966.
[70] B. Gürel, A numerical investigation of the melting heat transfer characteristics of phase change materials in different plate heat exchanger (latent heat thermal energy storage) systems, Int. J. Heat Mass Transf. 148 (2020) 119117, https://doi.org/10.1016/j.ijheatmasstransfer.2019.119117.
[71] W. Deng, J. Li, S. Samad, A.M. Abed, A. Almadhor, S. Alhumaid, et al., Optimization and prediction of heat absorption in a modular multi-section latent heat storage system with dome-shaped components using a multilayer perceptron model, TOPSIS analysis, and pareto fronts, J. Energy Storage 131 (2025) 117542, https://doi.org/10.1016/j.est.2025.117542.
[72] Q. Cui, T. Ning, C. Huang, C. Wu, J. Su, Design and operation of a novel cross fin in hot-water production system for buildings, Buildings 15 (2025) 320, https://doi.org/10.3390/buildings15030320.
[73] J. Vogel, M. Johnson, Natural convection during melting in vertical finned tube latent thermal energy storage systems, Appl. Energy 246 (2019) 38–52, https://doi.org/10.1016/j.apenergy.2019.04.011.
[74] Z. Esmaeili, S.M. Vahidhosseini, S. Rashidi, Enhancing latent heat thermal energy storage in triplex tube heat exchangers using tree-shaped fin structures with novel branching methods, J. Energy Storage 97 (2024) 112970, https://doi.org/10.1016/j.est.2024.112970.